

SO₂ DETECTION USING PLASMON DAMPING

By

ELI KASA TILAHUN

Bachelor of Science in Mechanical Engineering

Arba Minch University

Arba Minch, Ethiopia

2006

Submitted to the Faculty of the
Graduate College of the
Oklahoma State University
in partial fulfillment of
the requirements for
the Degree of
MASTER OF SCIENCE
December, 2012

SO₂ DETECTION USING PLASMON DAMPING

Thesis Approved:

Dr. A. K. Kalkan

Thesis Adviser

Dr. R. P. Singh

Dr. S. P. Harimkar

ACKNOWLEDGEMENTS

First and foremost, I owe my advisor, Dr. A. K. Kalkan a debt of thanks for his invaluable guidance and support throughout my graduate study. I was so lucky to have the opportunity to work for and learn from him. I would like to thank my defense committee members, Dr. R. P. Singh and Dr. S. P. Harimkar, too.

Thank you to my research colleagues in the Functional Nanomaterials Laboratory. I owe a great deal to Özge Topal for her help with Raman spectroscopy. Thank you very much to Sriharsha Karumuri for his assistance with TEM. I am grateful to Rama Krishna Ede and Ratan Putla who helped me get started on my project. I would also like to thank Lisa Whitworth for her assistance with AFM.

Finally, a special thank you goes to my family for everything they have done for me.

Name: ELI KASA TILAHUN

Date of Degree: DECEMBER, 2012

Title of Study: SO₂ DETECTION USING PLASMON DAMPING

Major Field: MECHANICAL AND AEROSPACE ENGINEERING

Abstract: The distinct optical properties of noble metal nanoparticles that stem from localized surface plasmon resonance (LSPR) have fascinated scientists for centuries. In recent years, frequency-shift LSPR sensors have been receiving intense attention for chemical/biological sensing. In this work, an SO₂ nanosensor based on a unique sensing mechanism, called hybrid plasmon damping, is developed. The active component of the sensor is a self-assembled monolayer of silver nanoparticles immobilized on a Si film. Nanoparticle synthesis is simple and low-cost, involving immersion of a Si thin film in a AgNO₃ solution. In addition, the sensor response is monitored in real-time by a hand-held UV-vis spectrometer. The optical extinction spectrum of the nanoparticles reports increase in the LSPR bandwidth that is primarily due to chemical interface damping, caused by adsorption of SO₂. This adsorbate-induced increase in damping ($\Delta\Gamma$) is demonstrated to be linearly proportional to the number of SO₂ molecules attached to the nanoparticle surface. Therefore, the increase in damping (i.e., LSPR bandwidth) is exploited to quantify the SO₂ concentration. The sensor detects 1 ppm SO₂ in less than a second and at an accuracy of 94.3 %. The present work also elucidates the chemisorption configurations of SO₂ to the Ag nanoparticles by surface-enhanced Raman spectroscopy.

TABLE OF CONTENTS

Chapter	Page
1. INTRODUCTION	1
2. BACKGROUND	6
2.1 Plasma oscillations and plasmons	6
2.2 Localized surface plasmon resonance (LSPR)	9
2.3 Hybrid-plasmon modes	13
2.4 Hybrid-plasmon damping sensing	14
2.5 Derivation of a relationship between $\Delta FWHM$ and $\Delta\Gamma$	16
3. METHODOLOGY	19
3.1 Silicon film deposition on glass	19
3.2 Silver nanoparticle synthesis	20
3.3 SO ₂ generation	22
3.4 Optical extinction measurements	23
3.5 Nanoparticles characterization	27
3.6 SO ₂ characterization	28
4. RESULTS AND DISCUSSION	29
4.1 Size and size distribution of Ag nanoparticles	29
4.2 Height of Ag nanoparticles	29
4.3 Extinction spectrum of Ag nanoparticles	32
4.4 SO ₂ adsorption to Ag nanoparticles	35
5. CONCLUSIONS	41
REFERENCES	43

CHAPTER 1

INTRODUCTION

Currently, the U.S. consumes around 20 million barrels (almost a quarter of the world's consumption) of petroleum per day [1, 2]. With an average of 13 billion ton-miles of freight shipments [3] and 13 billion passenger-miles of people travels [4], the transportation sector utilizes 70 % of this daily consumption [1]. A serious concern about such large fuel consumption is the emission of air pollutants at threatening levels. Harmful emissions, such as sulfur oxides (SO_x), nitrogen oxides (NO_x), carbon monoxide (CO), and particulate matter (PM) have profound effects on our health and the environment. For example, NO_x reacts with volatile organic compounds (VOCs) and forms smog, which is known to cause asthma, reduced lung function, emphysema, premature death and respiratory infections like pneumonia and bronchitis [5-10]. It also affects the environment for instance by damaging crops, producing acid rains and reducing visibility [11-15]. Consequently, smog exposure has been linked to higher emergency room visits, increased hospital admissions and more frequent work and school absenteeism [5, 16-18]. Given today's skyrocketing health care cost, which amounts to 18% of the nation's GDP [19], no doubt that vehicle emissions significantly impact the economy.

Gasoline- and diesel-powered vehicles are by far the major source of air pollutants. Most of the vehicles are fitted with advanced emissions control devices, such as catalytic converters and particulate filters. These devices are the keys in the reduction of atmospheric pollution by converting most of the NO_x , CO, and PM into harmless compounds. However, it has become apparent, over the years, that SO_x adversely deteriorate the performance of catalytic converters by reducing catalyst efficiency and competing with other emission species in chemical reactions, which otherwise convert exhaust NO_x , PM and CO into nontoxic compounds [20-23]. SO_x are also the precursors to acid rain, which causes corrosive wear on valve guides and cylinder liners, eventually resulting in premature engine failure [24-26]. As SO_x are byproducts of combustion of organosulfurs, maintaining low sulfur levels in fuels is critical in protecting the expensive catalysts and reducing the above-mentioned toxic exhaust emissions.

Prompted by these problems, government agencies in the U.S. and around the world have issued regulations calling for no higher than 15 ppm fuel sulfur level beginning in June 2006, a dramatic reduction from the former level of 500 ppm [27-30]. Under these standards, PM and NO_x will be reduced respectively by 110,000 and 2.6 million tons per year compared to the emissions under the precedent standard levels [27]. By using ultra-low sulfur fuels, U.S. Environmental Protection Agency (EPA) predicts that 5,500 chronic- and 17,600 acute-bronchitis cases, 360,000 asthma attacks and 8,300 premature deaths can be prevented every year. This would consequently save the nation around \$71 billion a year [27].

The aforementioned regulation, according to EPA, also imposes obligations to monitor the sulfur not only during production, but also at strategic transmission pipelines, storages and end-user distributors [27]. This is because the sulfur levels at the refineries do not exactly represent the levels at the end-users for a couple of reasons. First, the same transmission pipelines are used to transport different grade fuels with sulfur contents as high as 2000 ppm (jet fuel). It is highly probable, thus, some mixing could occur at the interface of two batches, 15 and 2000 ppm for

instance, degrading the quality of the low-sulfur material. Second, residual sulfur from high-sulfur fuel could contaminate subsequent low-sulfur material beyond the interface [27].

To this end, trace-level sulfur monitoring technologies are required by different entities ranging from the refineries to the fuel stations, to the government inspection laboratories in the efforts of insuring the true implementation of fuel sulfur limits, and most importantly, the health condition of emissions control devices. The best techniques to detect and measure sulfur levels seem those which directly employ the fuels in the liquid phase. However, it has been found out in the present work that detecting the hetrocyclic sulfur-containing compounds, like benzothiophene and dibenzothiophene, is very difficult owing to their low reactivity with metal nanoparticles. On the other hand, developing techniques that are aimed at monitoring the exhaust SO_x concentrations would offer twofold benefits. First, it helps to benchmark the emissions control device performance. Second, the SO_x concentrations at the engine-exhaust manifold have direct implications for fuel sulfur levels.

The objective of this thesis, accordingly, has been to develop a nanosensor, which is capable of monitoring SO_2 of concentrations as low as 1 ppm. The active component of the sensor is a monolayer of silver nanoparticles (NPs) immobilized on a glass substrate, i.e., the sensing element in Figure 1.1. The silver monolayer is synthesized using “nanometal-on-semiconductor” approach, a simple and low-cost technique involving immersion of silicon films in a silver nitrate (AgNO_3) solution. This innovative nanofabrication technique enables production of nanoparticles with interparticle separations as low as few nanometers without aggregation, resulting in strong electromagnetic interactions between the nanoparticles (i.e., hybrid plasmon modes).

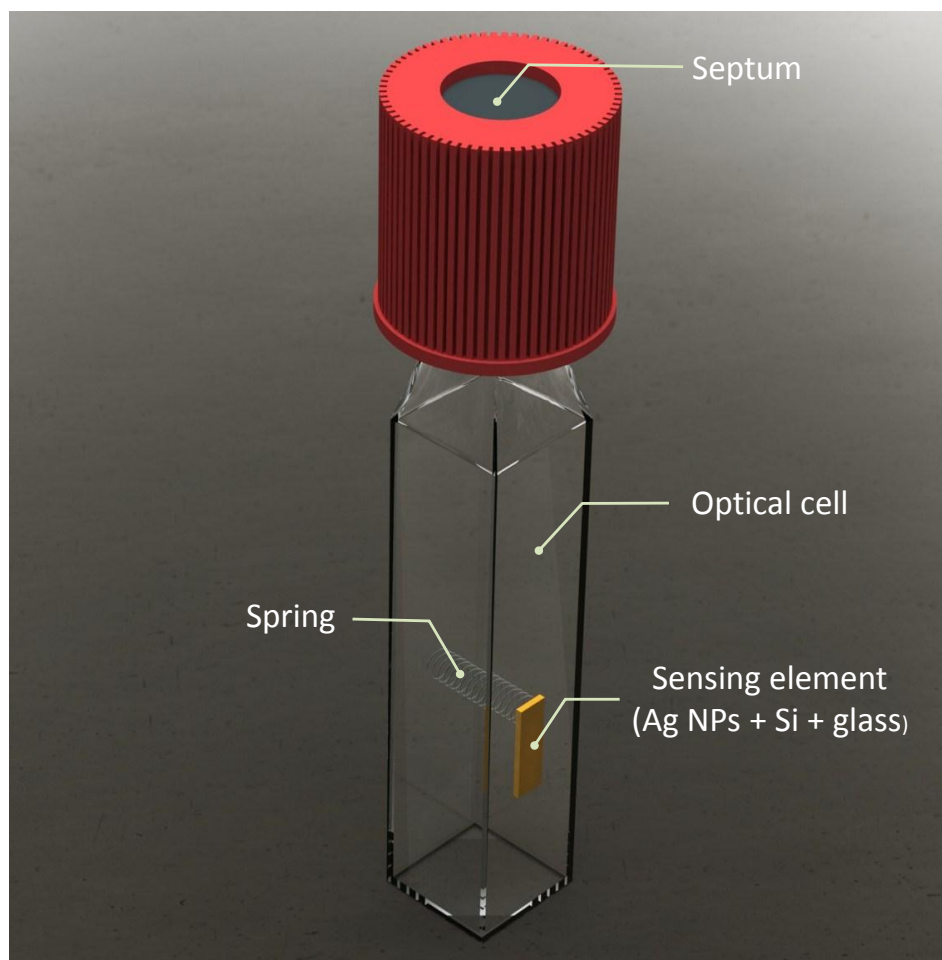


Figure 1.1 Drawing of the SO₂ sensor prototype developed in the present thesis showing the active sensing element.

When visible light is incident on a silver nanoparticle, collective oscillation of free electrons will set up. These collective oscillations account for a phenomenon called localized surface plasmon resonance (LSPR), which is described in Section 2.2. LSPR manifests itself as a broad and strong UV-visible extinction (absorption + scattering) band. The position, intensity and bandwidth of such extinction band are sensitive to particle size, shape, interparticle distance and refractive index of the surrounding medium. If the local refractive index around the nanoparticle is altered, for example due to chemical attachments to nanoparticle surface, the LSPR frequency changes. This frequency shift is usually measurable. One can utilize this property to detect and measure

analytes that have chemical or biological importance. As a matter of fact, frequency-shift LSPR sensors take advantage of this property.

This work, on the other hand, employs a superior and unique sensing mechanism, known as hybrid plasmon damping sensing (Section 2.4). When SO_x adsorb onto the silver nanoparticles, they broaden the width of the LSPR band in proportion to the number of SO_x molecules attached, primarily due to an effect called chemical interface damping (CID). It is this adsorbate-induced change in damping that is used as a sensing platform in the present thesis work.

The proceeding chapters are organized as follows. The next chapter details the background of the optical response of metal nanoparticles and the concept of dipolar and hybrid plasmon modes and their associated resonances. Chapter 3 is devoted to experimental procedures employed in the present thesis. Chapter 4 then presents and discusses the results that have been obtained. Finally, the conclusions drawn from this work are presented in Chapter 5.

CHAPTER 2

BACKGROUND

2.1 Plasma oscillations and plasmons

Metals can be treated as plasmas, consisting of fixed positive atomic cores surrounded by freely moving sea of electrons. The net charge of these ions and electrons at equilibrium is zero.

However, if there occurs, for example due to thermal fluctuations [31] or nearby passage of electrons [32, 33], a local displacement of electrons from equilibrium, the positively charged background left behind exerts a restoring force on the electrons. In so doing, the electrons pick up kinetic energy and overshoot their equilibrium positions. The positive background pulls the electrons back to their original mark, overshoot their equilibrium positions again, and so forth. As a consequence of this overshooting and subsequent charge neutrality restoration effort, collective electron gas oscillations, called plasma oscillations, will establish. Quanta of these oscillations are named as plasmons. Plasmon can be considered as the particle name for electron density waves, as photon is the particle name for electromagnetic (EM) waves. In general, two types of plasmon modes can be identified: bulk plasmons and surface plasmons.

Bulk plasmons are longitudinal oscillation modes within bulk metals. They oscillate with characteristic frequencies, called plasma frequencies, given by [34]

$$\omega_p = \sqrt{\frac{n \cdot e^2}{\epsilon_0 \cdot m}} \quad (2.1)$$

where n is the density of electrons, e and m are electric charge and mass of electron respectively, and ϵ_0 is the relative permittivity of free space.

This frequency plays a significant role in determining the optical properties of metals. If an incident light of frequency $\omega < \omega_p$ is incident on a bulk metal, it induces motion in the electron gas, thereby screening out the incident electric field and leading to a reflection. Incident light having a frequency greater than ω_p , on the contrast, can propagate through the metal because the electrons cannot respond fast enough to screen out the field. Most metals have their plasma frequencies in the UV spectral region, explaining why bulk metals reflect the visible portion of the electromagnetic radiation. One can substitute appropriate values into Equation 2.1 and find out that ω_p of metals are in fact in the UV.

Bulk plasmons, due to their longitudinal nature, cannot interact with light (a transverse wave) and can only be excited via particle collisions [35], such as electron bombardment [33]. As a result, they are not much of interest from an application standpoint.

Surface plasmons, on the other hand, are those plasma oscillations occurring at metal surfaces. Planar metal- and nanoparticle-dielectric interfaces are two geometries known to support surface plasmons. The planar metal-dielectric interface favors propagating surface plasmons, while the nanoparticle-dielectric interface supports localized surface plasmons (LSPs). In order to excite propagating surface plasmons by light, certain conditions need to be fulfilled. However, we are not concerned about propagating plasmon modes here. This work employs surface plasmons

confined to metallic nanoparticle surfaces (i.e., LSPs), to detect trace level SO₂ and measure its concentration. The resonant modes of localized surface plasmons will be described in Section 2.2.

In contrast to bulk plasmons, surface plasmons strongly interact with light, and hence resonance can occur if they are excited by the same. This coupling, in principle, results infinite amplitude at the resonant frequency. However, due to dissipative processes, such as electron and light scatterings, the electron gas oscillation experiences damping [36]. These dissipative properties, or more generally the optical responses of metals, are usually described using a frequency dependent, complex-valued dielectric function (relative permeability) of the free electron gas, which is given by [37]

$$\varepsilon(\omega) = \varepsilon_1(\omega) + i\varepsilon_2(\omega) \quad (2.2)$$

According to the Drude model of the optical response of metals, the real and imaginary components of $\varepsilon(\omega)$ in the long-wavelength limit (i.e., for $\omega \gg \Gamma$) are approximated as [37]

$$\varepsilon_1(\omega) \approx 1 - \frac{\omega_p^2}{\omega^2} \quad (2.3)$$

$$\varepsilon_2(\omega) \approx 1 - \frac{\omega_p^2}{\omega^3} \Gamma \quad (2.4)$$

where ω is the frequency of the applied electric field, $\Gamma = 1/\tau$ is a characteristic collision frequency (damping factor) and τ is an electron relaxation time (i.e., characteristic time interval between collisions that dampen the free electron gas oscillation) associated with the metal.

The real component of the dielectric function determines the amount of polarization induced by incident light (i.e., electric field), while the imaginary part describes the dissipation of energy inside the metal as a result of the polarization. In fact, $\varepsilon_2(\omega)$ is related to the absorption coefficient α of Beer's law [38], which determines the amount of absorption of the incident radiation within the metal.

2.2 Localized surface plasmon resonance (LSPR)

It has been briefly noted earlier that plasmons inside extended metals do not interact with incident electromagnetic waves in the visible spectral region. However, when the size of the metal is reduced significantly below the wavelength of incident light, the associated LSPs directly couple to the oscillating electric field of the exciting light (Figure 2.1), resulting in LSPRs. These resonances manifest themselves as intense UV-visible extinction bands in the vicinity of the resonant frequencies of the LSPs. A typical UV-visible extinction spectrum of silver nanoparticles is shown in Figure 2.2.

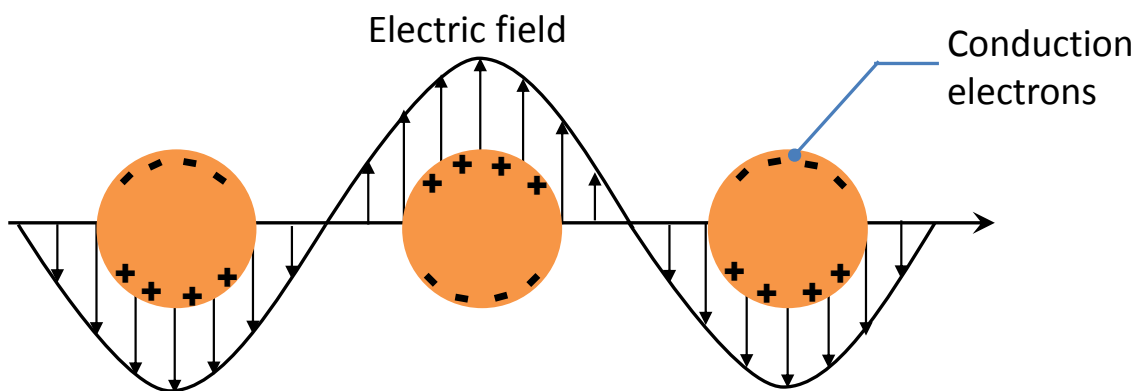


Figure 2.1 Schematic illustration of the LSP oscillations and dipole formation due to displacement of the conduction electron gas relative to the positive atomic cores.

The optical excitation of LSPs by incident light also leads to a significant increase in the electromagnetic field strength at the nanoscale-sized metal surface (metallic nanoparticles). This electromagnetic enhancement accounts for another related plasmonic phenomenon, called surface-enhanced Raman scattering (SERS). SERS is a phenomenon that dramatically enhances the intensity of the normally weak Raman scattering of a molecule on the surface of metallic nanoparticles by up to 10^{14} - 10^{15} times [39]. The normal Raman scattering represents only one inelastically scattered photon out of 10^8 elastically scattered photons [40]. SERS made Raman spectra measurements, detections and characterizations of single molecules a reality [41].

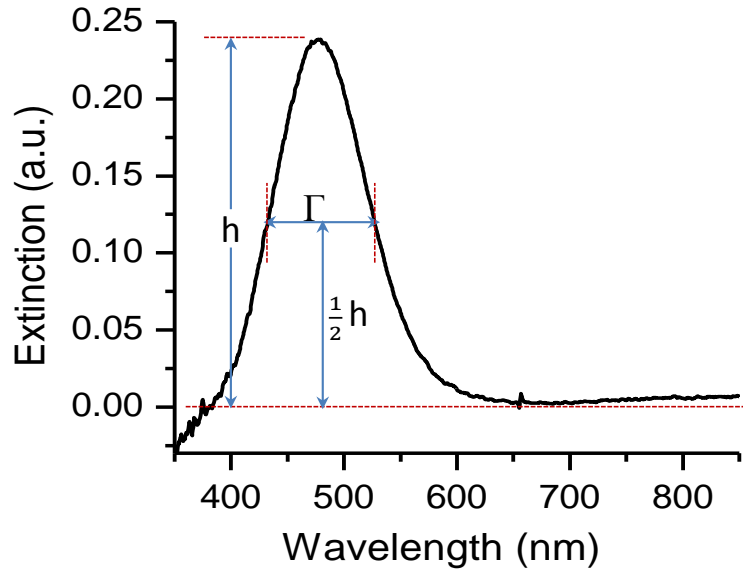


Figure 2.2 Extinction spectrum acquired from a monolayer of silver nanoparticles showing the plasmon resonance. h is extinction height, and Γ is the full width at half maximum (FWHM).

Wavelength, intensity and the bandwidth of LSPR in a nanoparticle are dependent on the dielectric function of the metal, particle size and shape, and the surrounding medium [42, 43]. Consequently, the spectral features of the LSPR can be tailored by adjusting the size, geometry and material of the nanoparticle as well as changing the surrounding dielectric medium of the particle [44, 45]. It is not difficult to tune, for example, the peak frequency from the UV through the visible, and into the IR spectral region just by changing the particle size or its shape.

This dependence of LSPR on the above-presented parameters has made metal nanoparticles exhibit distinct optical properties that do not exist in their bulk counterparts. For instance, the transmitted color of gold colloids changes from golden to blue, purple or red upon reduction of its size from approximately 200 nm through 30 nm [46]. Silver colloids appear yellow, red, or blue, depending on their size. The nanoparticles owe their unique colors, and most of their properties for that matter, to a selective, strong light scattering at resonant frequencies (singular resonance frequencies) as opposed to the corresponding bulk metals, which weakly absorb across the entire visible spectrum [46]. In fact, the sensitivity of the plasmon resonance frequency to local

refractive index and nanoparticle separation is the basis for a number of interesting applications, including bio/chemical sensing [47-53] and signal transduction [54, 55].

As will be discussed in Section 2.4, in order LSPR to occur in any material, the real part of the dielectric function of the material is required to be negative. Due to their high plasma frequencies and high density free electrons, metals generally provide the desired negative real dielectric functions. However, most metals suffer from inherently large losses in and near the visible wavelength range mostly due to interband electronic transitions. Owing to their relatively low damping factors (i.e., losses), noble metals, particularly silver ($\Gamma = 0.02$ eV [56]) and gold ($\Gamma = 0.07$ eV [56]) show a markedly well-resolved and high intensity extinction spectrum bands, making them highly suitable for plasmonic applications. Furthermore, plasmon resonances of silver and gold are located in the visible spectral region, enabling the effect of LSPR observable by the naked eye as a result of color formation. On this account, these metals are usually regarded as the best plasmonic metals.

The application of unique optical properties of metal nanoparticles dates back to the Romans. The antique Lycurgus cup (4th century A.D.), which looks red or green under transmitted or reflected light respectively (Figure 2.3 [57]), is one famous example that demonstrates the utilization of nanoparticles in the pre-18th century [58, 59]. Also, in the Medieval period, glassblowers and artists used stained glasses in decorating the windows of churches and in educating people via pictures (since there were no alphabets). The red- and yellow-colored stained glasses are later attributed to gold- and silver-colloids. Nonetheless, it was only in 1857, when Faraday systematically studied gold colloids and reported his results, that our understanding of the origin of their unique properties started to evolve [60].

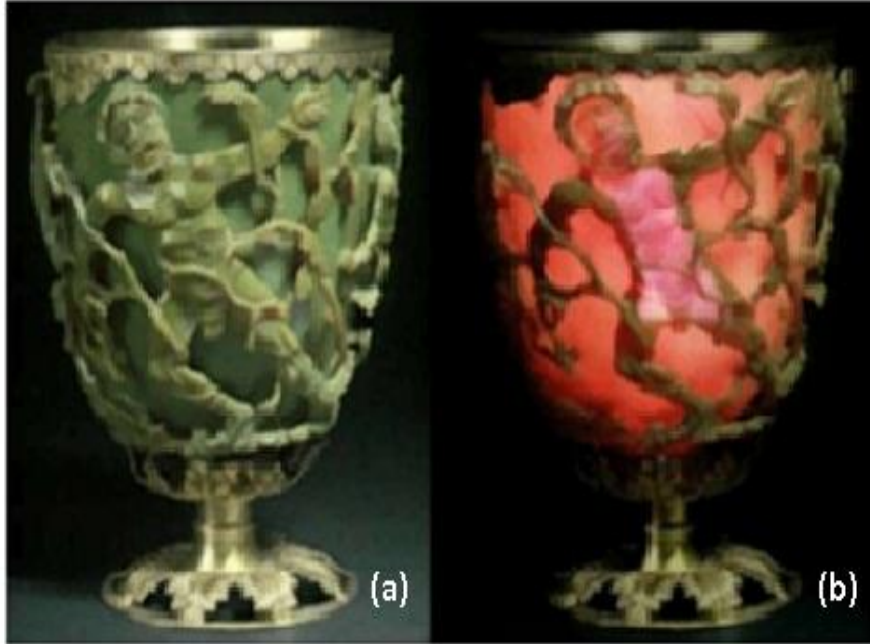


Figure 2.3 The Lycurgus cup, a fascinating example of metallic nanoparticles at work: (a) appearing green under reflected light; (b) looking red under transmitted light [57].

In 1908, following Faraday’s pioneering work, Mie solved Maxwell’s equations specifically for spherical nanoparticles and came up with an exact analytical solution to the extinction cross-

section, which is given by Equation 2.5 [61]. Extinction cross-section, σ_{ext} is defined as

$P_{\text{ext}} = \sigma_{\text{ext}} \cdot I$, where P_{ext} is the total electromagnetic power absorbed and scattered by the nanoparticle (extinct power) and I is the intensity of the electromagnetic field. The Mie theory has significantly deepened our theoretical insight of particle-light interactions, and has made modeling the optical properties of nanoparticles possible.

$$\sigma_{\text{ext}}(\omega) = 9 \frac{\omega}{c} \varepsilon_m^{3/2} V_0 \frac{\varepsilon_2(\omega)}{[\varepsilon_1(\omega) + 2\varepsilon_m(\omega)]^2 + \varepsilon_2(\omega)^2} \quad (2.5)$$

where ω and c are the frequency and speed of light respectively, ε_m is the dielectric function of the local environment around the nanoparticle, V_0 is the volume of the nanoparticle, and ε_1 and ε_2 hold their previous meanings of Equations 2.3 and 2.4.

Fast-forward to the last quarter century, the interest in nanotechnology has soared. The significant number of papers that have been published on metal nanoparticles in this period justifies the same [62]. This, of course, is due to the high improvements that have been achieved in measurement and computational techniques [58], which in turn has led scientists to be able to observe, manipulate and structure matter at nanoscale dimensions. Today, nanoparticles are being appreciated for their potential applications among a wide range of disciplines. One can find applications of nanoparticles in chemical and biological sensing [47-53, 63], medicine (e.g., cancer treatment [64-66], drug delivery [67, 68], medical diagnosis [69, 70], imaging [71, 72]), environmental science [73], information technology [74, 75], energy storage and conversion [76, 77], and a variety of consumer goods like clothing, cosmetics and sporting goods [73].

2.3 Hybrid-plasmon modes

A single metal nanosphere is characterized by dipolar plasmon mode. However, when two or more nanoparticles are brought close to one another (i.e., less than a particle diameter apart), their individual dipole near-fields couple or interact to form new, hybridized plasmon modes in a way analogous to the molecular orbital formation from atomic orbitals [45, 78, 79]. For example, two single-particle plasmons can interact in two ways, symmetric and anti-symmetric oscillations, resulting in two hybridized plasmon modes. These symmetric and anti-symmetric oscillations can be regarded as bonding and anti-bonding combinations. The former appears at lower energy than the corresponding dipolar mode (Figure 2.4a), while the latter corresponds to the higher energy case (Figure 2.4b) [46, 80]. The anti-symmetric hybrid mode is usually called dark plasmon owing to its unobservable nature. This is because the interacting dipole near-fields cancel each other and the net dipole moment of the associated combination mode becomes zero [80]. One could view the anti-symmetric oscillation mode as destructive interference of waves. The symmetric oscillation mode, however, is observable upon excitation by light, and unsurprisingly is known as bright plasmon.

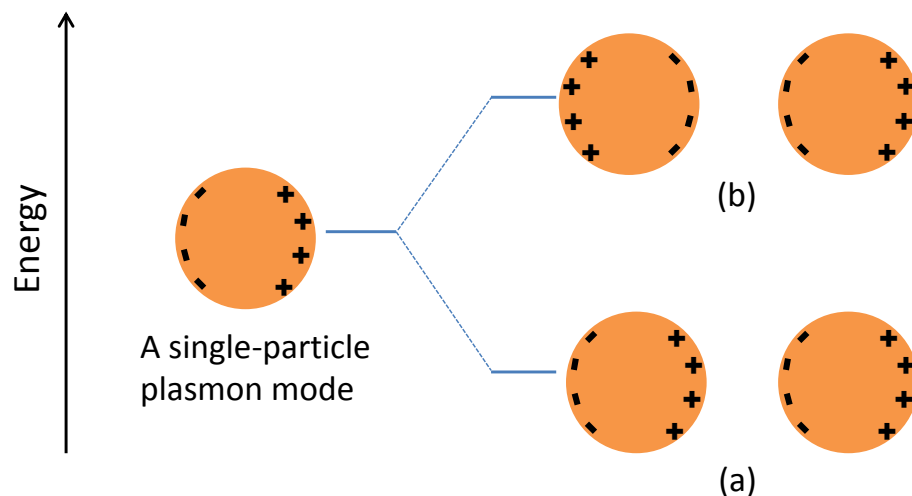


Figure 2.4 Schematic representation of the interaction of two single-particle plasmons in order to form two hybridized plasmon modes: (a) symmetric oscillation mode; (b) anti-symmetric oscillation mode.

In this work, we utilize the change in hybrid plasmon properties due to SO_2 adsorption, specifically the hybrid plasmon damping (Section 2.4), as the sensing mechanism for a couple of reasons. First, it is much easier to fabricate and work with particle ensembles than a single nanoparticle or arrays of non-interacting particles. Here, we employ a monolayer of silver nanoparticles synthesized using “nanometal-on-semiconductor” technique (Section 3.2), which presents an intense hybrid plasmon extinction peak. Second, the hybrid plasmon extinction peak is found to exhibit a higher chemical sensitivity (i.e., larger damping increase in response to molecular adsorption) than the dipole mode [81-83].

2.4 Hybrid-plasmon damping sensing

As previously pointed out, the characteristics of LSPR, such as its peak frequency, are sensitive to the particle size, shape, surrounding medium, etc. This sensitivity is of outstanding interest because one can utilize it for different sensing applications. For example, bound molecules of chemical or biological importance could be detected by studying the change in the local refractive index, which in turn induces a measurable peak frequency shift. Indeed, this dependence of the

resonance frequency on the surrounding refractive index (dielectric function) can be extracted from Equation 2.5. According to this equation, the strongest optical response of the nanoparticle (i.e., the extinction maximum) occurs when the denominator is minimal. This situation is satisfied evidently when $\epsilon_1(\omega) \approx -2\epsilon_m$, provided variation of $\epsilon_2(\omega)$ is sufficiently small. The condition $\epsilon_1(\omega) \approx -2\epsilon_m$ implies that the frequency at which the extinction maximum appears changes when the dielectric function ϵ_m of the local environment is altered, for example due to chemical attachments on the particle surface. In fact, this is the principle behind frequency-, or equivalently, wavelength-shift LSPR sensors. An alternative sensing mechanism to the wavelength-shift LSPR sensing, which also employed in this work, is utilizing the change in hybrid-plasmon damping induced by adsorption of chemical species on the particle surface.

The intrinsic damping (homogeneous broadening), Γ of single-particle plasmon has been introduced in Equation 2.4. Various radiative as well as non-radiative dissipative processes account for this damping. The radiative damping accounts for light scattering, i.e., decay of plasmon to photons. The non-radiative damping, however, results from a scattering of the collectively oscillating electrons at defect sites, nanoparticle surfaces, impurities, etc [61, 80]. The effect of such electron scatterings is eventually to decay the LSPR to phonons (heat).

Theoretically, the intrinsic damping is equal to the full width at half maximum (FWHM) of the extinction peak of the single particle. However, for an ensemble of particles, the extinction peak also subjects to heterogeneous broadening (distribution) [81], for instance due to distribution of particle sizes, shapes and spacings [84, 85].

Another very important mechanism that contributes to the heterogeneous broadening is the so-called chemical interface damping (CID), which results from chemisorption of atoms or molecules to the nanoparticle surface [86-89]. This adsorption of molecules onto the particle surface introduces new electronic states [81, 86]. If certain electrons that contribute to the LSPR

transfer into and out of these adsorbate-induced electronic states (dynamic charge transfer [86]), the coherent motion of the whole conduction electrons of the oscillating electron density gets disturbed, resulting in plasmon decay and broadening of the LSPR. This broadening is found to be directly proportional to the number of adsorbates on the particle surface [80]. As a result, CID can be a valuable sensing tool for monitoring chemical interaction of analytes with the nanoparticle surface.

Due to the above described heterogeneous broadening, FWHM does not directly represent the damping factor, Γ . Nevertheless, one can derive an equation that relates the change in FWHM (ΔFWHM) due to chemical adsorptions and the associated change in Γ ($\Delta\Gamma$) as presented below. In the present thesis work, we adopt this relationship to determine SO_2 concentration.

2.5 Derivation of a relationship between ΔFWHM and $\Delta\Gamma$

In principle, a single-particle plasmon is expected to have a resonance peak of Lorentzian shape. The measured extinction peak was rather found to be Gaussian as validated by fitting the experimental data to Gaussian function using Origin 8.1 software. As can be seen from Figure 2.2, the representative experimental extinction spectrum has a much wider FWHM than a typical Lorentzian peak due to the forenamed heterogeneous broadening effects, i.e., the measured FWHM is the combination of both homogeneous- and heterogeneous broadenings. The Gaussian nature of the observed extinction peak may be understood as the envelope function of the multiple Lorentzian peaks that are convoluted together.

The convoluted form of Lorentzians by a Gaussian envelope, by definition, is Voigt function. To obtain a relationship between the FWHM and the damping factor (Γ), we start by fitting the experimental data to this Voigt function, which is given by [90]

$$V(\omega) = \int_{-\infty}^{+\infty} G(\omega_0)L(\omega - \omega_0)d\omega_0 \quad (2.6)$$

where ω_0 is the peak frequency of a Lorentzian.

The Gaussian function with a standard deviation of σ is given by

$$G(\omega_0) = \frac{e^{-\omega_0^2/2\sigma^2}}{\sigma\sqrt{2\pi}} \quad (2.7)$$

The FWHM of the Gaussian peak, FWHM_G and the Lorentzian function, $L(\omega - \omega_0)$ are presented in Equations 2.8 and 2.9 respectively.

$$\text{FWHM}_G = 2\sigma\sqrt{2\ln(2)} \quad (2.8)$$

$$L(\omega - \omega_0) = \frac{\Gamma/2\pi}{(\omega - \omega_0)^2 + \Gamma^2/4} \quad (2.9)$$

where Γ is the damping factor (FWHM) of a single-particle Lorentzian peak. After appropriate substitutions and rearrangements, the FWHM of the Voigt profile that is largely of Gaussian nature is approximated as [90]

$$\text{FWHM}_V \approx 0.53\Gamma + \sqrt{0.21\Gamma^2 + \text{FWHM}_G^2} \quad (2.10)$$

Now, an equation that relates the change in the Lorentzian FWHM ($\Delta\Gamma$) and the change in the Voigt FWHM (ΔFWHM_V) is required. This can be achieved by employing a linear differential approximation as follows

$$\Delta\text{FWHM}_V = \frac{d\text{FWHM}_V}{d\Gamma} \Delta\Gamma = [0.53 + 0.5(0.42\Gamma)(0.21\Gamma^2 + \text{FWHM}_G^2)^{-1/2}] \Delta\Gamma \quad (2.11)$$

One may rewrite the above equation as

$$\Delta\text{FWHM}_V = [0.53 + 0.5(0.42\Gamma)\left(\frac{1}{\text{FWHM}_G\sqrt{0.21(\Gamma/\text{FWHM}_G)^2 + 1}}\right)] \Delta\Gamma \quad (2.12)$$

By noting that $\Gamma \ll \text{FWHM}_G$ (as a result of the Voigt fit being dominantly Gaussian), Equation 2.12 can be reduced to

$$\Delta\text{FWHM}_V \approx [0.53 + 0.21(\Gamma/\text{FWHM}_G)]\Delta\Gamma \quad (2.13)$$

By re-employing the fact that $\Gamma \ll \text{FWHM}_G$, one will be able to further simplify Equation 2.13 to

$$\Delta\text{FWHM}_V \approx 0.53(\Delta\Gamma) \quad (2.14)$$

Equation 2.14, thus, represents the relationship between the change in extinction peak width and the change in damping factor.

CHAPTER 3

METHODOLOGY

3.1 Silicon film deposition on glass

Si thin films were deposited on Corning 1737 glass substrates by plasma-enhanced chemical vapor deposition (PECVD). The primary function of Si is to reduce ionic silver (Ag^+) in AgNO_3 solution to neutral atomic silver, and subsequently produce silver nanoparticles. The Si film immobilizes nanoparticles on the glass so that no additional linking agent is required. This binding action is owed to charge transfer between Ag particles and Si film, leading to Columbic attraction between the nanoparticles and the glass [80].

Prior to the film deposition, the glass substrates were thoroughly cleaned in order to remove any foreign particulates and contaminants from the surface. The following five cleaning steps were followed in their consecutive order. 1) The glass was soaked in ultrasonically agitated deionized (DI) water for 5 min at 25 °C, and then rubbed with nylon brush to mechanically remove dust particles of macroscopic scale. The DI water used here, and in any subsequent experimental procedures throughout the present thesis work, was polished to a resistivity of 18.2 M Ω . 2) The glass was ultrasonicated again for 10 min in a 2:3 ratio of isopropyl alcohol (IPA) and DI water

solution. This step was conducted to get rid of any organic contaminants. 3) Ultrasonication in DI water was conducted once more for 10 min to remove IPA and/or organic material residues from the glass surface. 4) The glass was then rinsed several times with DI water to further flush away any residual contaminants. 5) Finally, it was blow dried with argon stream at 30 psi. The blow-drying was performed to avoid water droplets from drying on the glass, thereby providing clean and spot-free surface. In order to further ensure that no adsorbed water was remained on the surface, the glass was heated at 150 °C for 10 min on a VWR 500 Series hot plate.

Plasma-Therm 790+[®] PECVD system was employed for depositing the Si films. The system generates the plasma between two capacitively coupled, parallel aluminum plates. The silicon was deposited from silane (SiH₄) and helium gases of 1:99 mixture ratio. These precursor gases were injected into the deposition chamber through an overhead shower head at a flow rate of 1200 sccm. Subsequently, the silicon was deposited onto the cleaned glass placed on the 667 mm diameter stage (electrode) of the PEVCD system that was heated to 250 °C. The system was operated at excitation radio frequency of 13.56 MHz and output power level of 100 W. The deposition was performed at an approximate deposition rate of 0.15 nm/s until about 50 nm film thickness was obtained. The base and process pressures of the chamber were maintained at 10^{-6} and 1 Torr, respectively.

3.2 Silver nanoparticle synthesis

The Ag nanoparticles were synthesized using “nanometal-on-semiconductor” technique [80]. This method involves basically immersion of semiconductor film deposited on glass in metal salt solution for a given period of time, thereby reducing the metal ions present in the solution to their neutral atomic form. The metal atoms subsequently grow to nanoparticles on the Si surface. A monolayer of nanoparticle synthesized using this approach provides a highly sensitive sensing platform with a rapid response time compared to those particles synthesized using conventional

colloidal reduction techniques. This is because conventional colloidal reduction techniques employ surfactants and capping agents for the purpose of controlling sizes of the nanoparticles and preventing them from aggregating. The presence of such agents on the surfaces of particles impede molecular adsorption as well as increases the intrinsic damping described in Section 2.4, and consequently reduces the sensitivity of the sensing element [80].

In this work, the Ag nanoparticles were synthesized by immersing the Si film deposited on glass (Section 3.1) in a 0.002 M AgNO₃ + 0.1% HF solution. The HF was added in the solution for etching silicon oxide that is produced during oxidation reaction. In this procedure, the substrate was first cut into 5×15 mm² pieces. By using a diamond tipped scribe (glass engraving pen), the glass was first scored on the non-film side. In order to make a clean break, the score was then run from one edge to the other using a Fletcher running plier. While making the score on the substrate, the film side was kept down on a 4" H22 Series twist-lock Fluoroware[®] polypropylene sample holder (wafer carrier). The sample holder is designed to have a concave surface so that the film side of the substrate only contacts it at the corners; thereby, the Si film surface is kept untouched and ultraclean.

As depicted in Figure 3.1, the specimen was then held on its edge in a flat tip tweezers (not shown in the figure), and immersed in AgNO₃ solution dispensed into a 20 mL polystyrene antistatic pour boat (weighing dish) for 20 s. In order to facilitate reduction of Ag ions and growth of nanoparticles, the substrate was turned upside down just prior to immersion, i.e., the film side of the substrate was kept up during the reaction. The substrate was also held in the tweezers throughout the whole synthesizing process. After the 20 s immersion time, the sample (Ag NPs + Si + glass) was immediately dipped in a beaker of DI water to stop the reaction. Subsequently, the sample was blow dried using ~15 psi argon stream to prevent water droplets from drying on the sample.

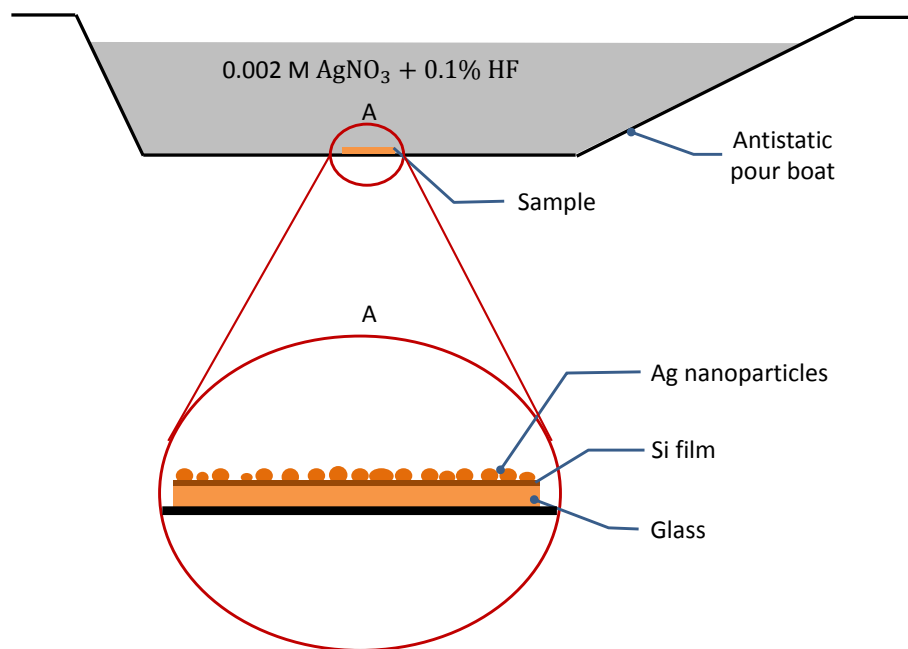
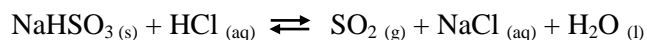


Figure 3.1 Schematic illustration of Ag nanoparticle synthesis.

3.3 SO₂ generation

SO₂ was generated within a 10 mL Luer-Lok™ Tip gas-tight syringe using “In-Syringe Method” [91]. In this procedure, 300 mg of A.C.S reagent grade sodium bisulfite (NaHSO₃) (Sigma-Aldrich), was placed into a plastic vial cap (Educational Innovations Inc.), and was lowered into the bottom of the syringe barrel without spilling the NaHSO₃. Floatation was used to lower the vial cap (i.e., by sealing the barrel hole with finger, the barrel was filled with water. The vial cap containing the NaHSO₃ was then floated and lowered into the bottom of the barrel by releasing the seal made by finger). After resting the cap on the bottom of the barrel and replacing the plunger, 3 mL of 6 M HCl was drawn into the syringe. While maintaining the syringe in vertical position, a lever activated syringe valve (MTB Sampling Valve) with a short connecting tube was installed. The syringe was then gently shaken up and down in order to mix the reagents and start the reaction. The reaction is given by



By using a 22 gauge needle, 2 mL of pure SO₂ was injected into a 250 mL air-filled glass bottle at 1 atm pressure in order to obtain 4000 ppm of SO₂. The bottle was sealed with a gas-tight VWR rubber stopper, and the syringe was turned upside down to avoid the liquid reaction mixture from being transferred into the bottle. This 4000 ppm SO₂ sample was further diluted in air to 100, 25, 5, and 1 ppm sample concentrations by injecting the appropriate volumes of SO₂ into 250 mL glass bottles (for 100 and 50 ppm) and 5 mL optical cells (for 5 and 1 ppm). The optical cells were sealed with a gas-tight septum screw cap.

3.4 Optical extinction measurements

For extinction measurements and sensor development, the sample was enclosed in an optical cell as depicted in Figure 3.2. Prior to enclosing the sample, the optical cell was thoroughly cleaned. To begin the cleaning procedure, the optical cell was first filled with a 2:3 ratio of IPA and DI water solution, and sonicated for 10 min at 25 °C. After disposing the IPA/DI water solution and rinsing about 10 times with DI water, the cell was filled just with DI water. Subsequently, it was ultrasonicated again for another 10 min. Once the sonication was completed, the optical cell was rinsed again with DI water for at least 10 times, and blow dried with argon stream at 30 psi. Finally, the sample was securely fixed to the interior surface of the optical cell using a stainless steel spring. The center of the sample was positioned 15 mm from the optical cell's base so that the center of the sample aligns with the center of the incident light beam as shown in Figure 3.2.

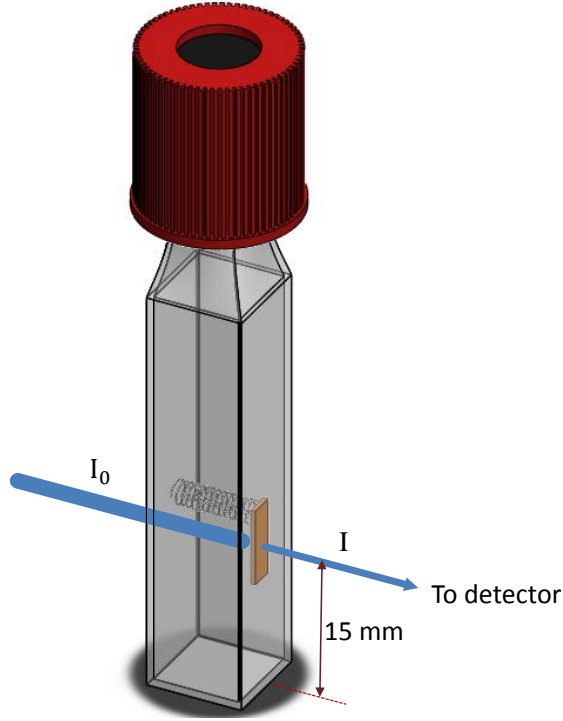


Figure 3.2 Illustration of the sensor prototype sample prepared for optical extinction. I_0 and I are incident and transmitted light intensities, respectively.

StellarNet EPP 2000C UV-vis spectrometer was utilized to measure the extinction spectrum of silver nanoparticles. The key component of the spectrometer is the CCD (charge-coupled device) detector. The CCD receives light transmitted through the sample as input and converts it into electronic signal in proportion to the intensity of the transmitted light. The output signal generated by the CCD is then processed by SpectraWiz[®] software. The software converts this output signal into a much valuable data format and presents it to the user in various forms such as extinction, transmission, reflectance and irradiance. In the present work, the data were recorded using the extinction mode. The extinction (E) is defined as the negative logarithm of the transmission coefficient (T), where the transmission coefficient is the ratio of the transmitted (I) and incident (I_0) light intensities. i.e.,

$$E = -\log(T) \quad (3.1)$$

$$\text{where } T = \frac{I}{I_0} \quad (3.2)$$

In most cases, only the extinction, and hence the transmission coefficient, of the Ag nanoparticles is of particular interest. Equation 3.1 represents, however, the total extinction, including extinctions by the Si film and the glass. Thus, to measure just the extinction spectrum of the Ag particles, the extinction of the substrate needs to be subtracted from the total extinction. This is achieved by measuring the extinction of a reference substrate. The reference is prepared by replacing the sample with a silicon-coated glass substrate in Figure 3.2. Hence, extinction of Ag nanoparticles is given by

$$E = E_{\text{sample}} - E_{\text{reference}} \quad (3.3)$$

where sample refers to Ag NPs + Si + glass and the reference refers to Si + glass. Both sample and reference measurements were obtained by subtracting the dark thermal signal baseline. Schematic setup of the system, i.e., the spectrometer and accessories, employed for the extinction measurement is presented in Figure 3.3.

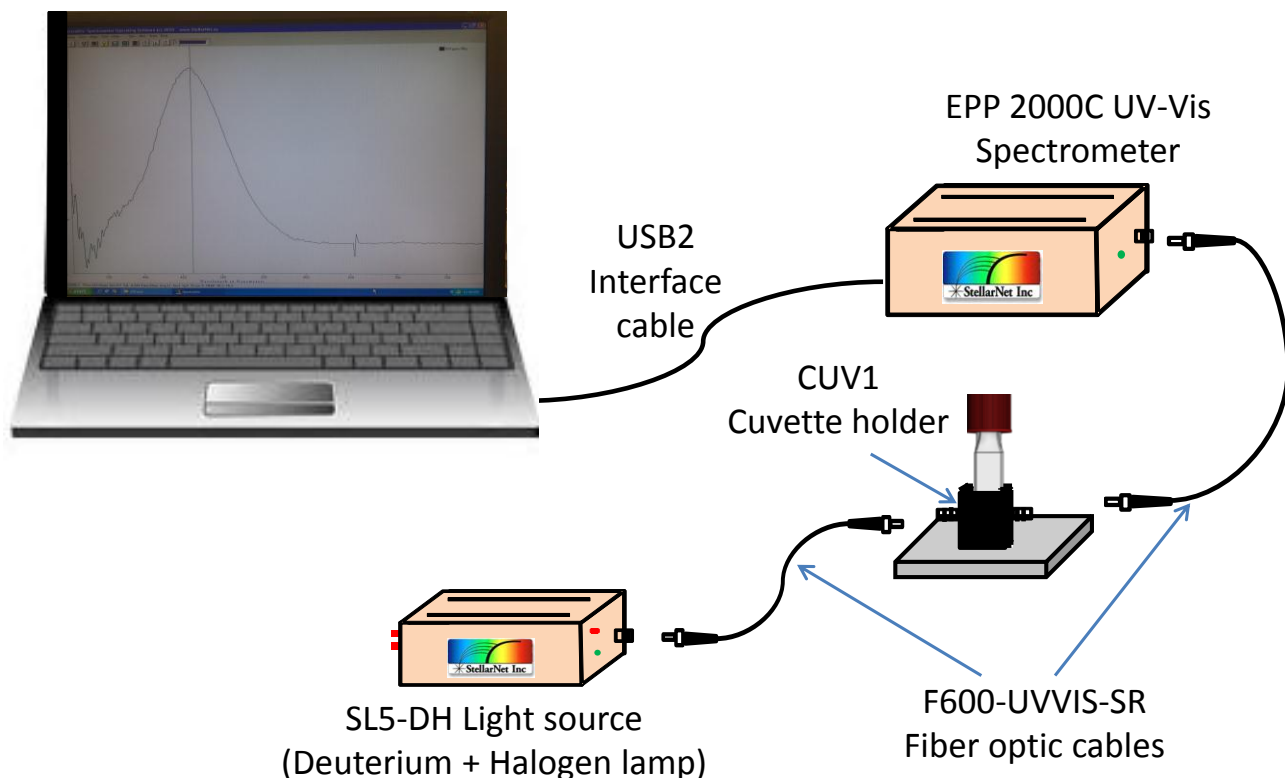


Figure 3.3 Schematic illustration of the optical extinction measurement setup.

Once the sample and reference were prepared and the spectrometer and accessories were connected, the SpectraWiz software was opened in scope mode. With the reference in place, the integration time and number of scans to average were adjusted to 100 ms and 5, respectively. Subsequently, with the light source off, a dark scan was collected. After saving the dark scan, the light source was turned on and a reference spectrum was taken. Finally, the system was switched into extinction mode, the reference was replaced by the sample, and then data collection was performed in the wavelength range of 300 and 850 nm.

Samples were prepared as shown in Figure 3.2 for different SO₂ concentration exposures. Extinction spectra of Ag nanoparticles were then recorded in response to air (i.e., 0 ppm SO₂) and 1, 5, 25, and 100 ppm SO₂ concentrations prepared as described in Section 3.3. Three replications were conducted for each of the concentrations. A 22 gauge needle and a 5 mL Luer-Lok gas-tight

syringe were employed for injecting SO₂ into the optical cells. Prior to SO₂ exposure, most of the existing air in the optical cell was drawn out by using a syringe. However, despite this withdrawing effort, the real concentrations are evidently less than the reported concentrations. Extinction spectra of the SO₂-exposed samples were collected within approximately 30 s period of time after the samples were exposed to SO₂.

The data were subsequently exported into Origin 8.1 software for analysis. FWHM was then extracted by fitting the spectral data to Gaussian function. The data was found to fit the Gaussian function very well (i.e., an average adjusted R-square value of 0.997). By comparing the FWHMs of the SO₂-exposed and the corresponding unexposed samples we were able to determine the changes in the FWHMs of all the concentrations investigated in this work. These changes in FWHMs were later employed to calibrate the sensor.

3.5 Nanoparticles characterization

Atomic Force Microscopy (AFM) and Transmission Electron Microscopy (TEM) were conducted to determine the size and size distribution of Ag nanoparticles. AFM images were recorded using a Veeco Multimode scanning probe microscope (Veeco, NY, USA) operating in tapping mode. The image was acquired over scan area of $1 \times 1 \mu\text{m}^2$. The scanning was conducted at a rate of 1Hz using NSC14 silicon nitride (Si₃N₄) tip cantilevers (MikroMasch, CA, USA). For the TEM imaging, a JEOL JEM-2100 scanning transmission electron microscope system (JEOL Ltd., Tokyo, Japan) was employed. The TEM system was operated at an acceleration voltage of 200 kV.

As-synthesized sample (Ag-on-Si-on-glass) was used for the AFM imaging. However, additional sample preparation was performed prior to collecting the TEM images. To begin, Ag nanoparticles were synthesized as described in Section 3.2. In order to lift off the Ag nanoparticles of the Si-on-glass substrate, the sample was immersed in a 5 mM solution of 1-

Octadecanethiol (ODT, MW 286.6) for 32 h. The ODT solution was prepared by dissolving 171.94 mg ODT in 120 mL of anhydrous ethanol. Subsequently, the dispersed particles in ethanol were dispensed onto a lacey-carbon-coated copper support grid to perform the TEM imaging.

3.6 SO₂ characterization

For this work, SO₂ was prepared as described in Section 3.3. To verify that the gas generated in Section 3.3 was indeed SO₂ and it adsorbs to nanoparticles, chemical characterization was conducted using a WITec alpha300 R confocal Raman microscope equipped with a UHTS 300 spectrometer. The Raman spectroscopy system utilized an Nd:YAG excitation laser of wavelength 532 nm. The system was operated at 1 mW power, and the laser spot size was 30 μm. The Raman scattered light was collected in back scattering configuration with a 20× lens of 0.4 numerical aperture focused on the Ag nanoparticle layer of the sample that is configured as shown in Figure 1.1. Raman spectra were collected from several different locations along the sample surface.

CHAPTER 4

RESULTS AND DISCUSSION

4.1 Size and size distribution of Ag nanoparticles

To determine size and size distribution of Ag nanoparticles, TEM samples were prepared as described in Section 3.5. Figure 4.1 shows a representative TEM image. In addition, the associated particle size distribution is shown in the inset of the figure. The size distribution was determined by the image processing software, MBF-ImageJ (MacBiophotonics ImageJ). The diameter of the nanoparticles was found to be 15 ± 6.8 nm. The total number of particles counted and analyzed by the software was 864.

4.2 Height of Ag nanoparticles

For particle height measurement, AFM height scans were obtained as described in Section 3.5. Figure 4.2 provides a representative AFM image. The height of the nanoparticles was then computed using the image processing software, NanoScope Analysis (Bruker Corporation). The average particle height was found to be 8.6 nm. The AFM image was also used for particle size determination on the xy-plane. The average particle size measured from the AFM image was approximately 20 nm, a higher value than the one acquired from the TEM image.

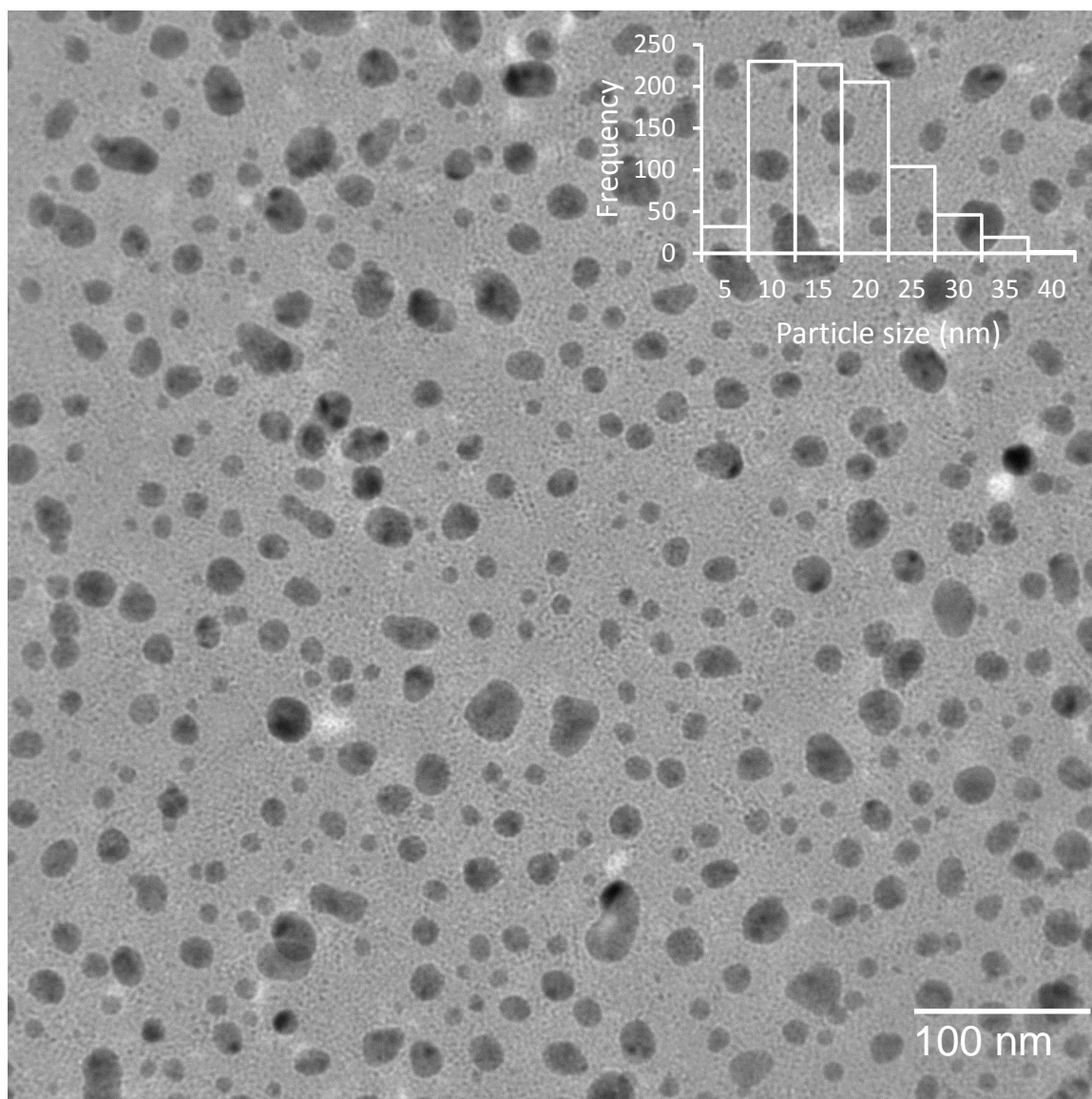


Figure 4.1 TEM image of Ag nanoparticles, and the associated particle size distribution. The image was taken after the nanoparticles were lifted off of the glass substrate using ODT and dispensed onto carbon-coated copper support grid.

This size difference stems from a tip-generated artifact (i.e., lateral resolutions or widths of features on AFM image depend upon the sharpness of the tip). As such, the cantilever tip (probe), which is usually pyramidal in shape, yields artificially larger particle size than the real size. In addition, the bluntness of the tip further increases the measurement error.

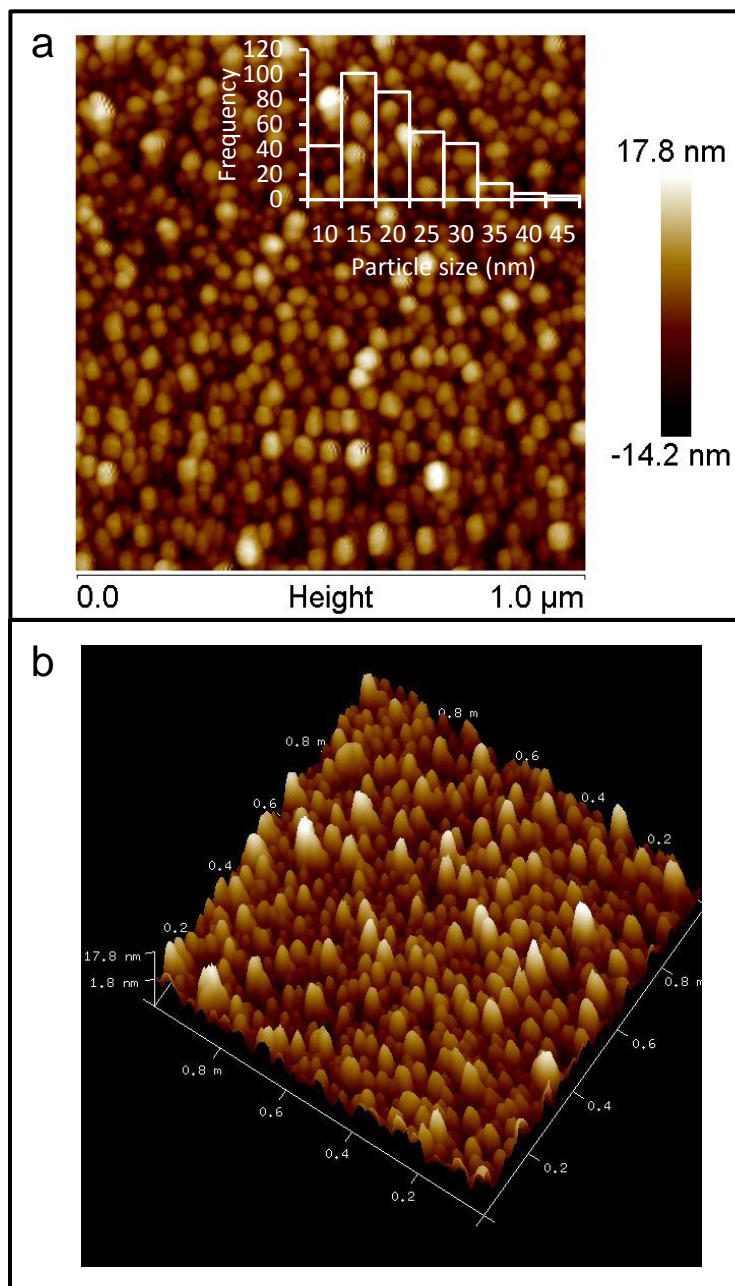


Figure 4.2 AFM image of Ag nanoparticles: (a) particle size and the associated size distribution; (b) Oblique angle image of the Ag nanoparticles that is generated from the same data as in (a).

4.3 Extinction spectrum of Ag nanoparticles

Optical extinction spectra of Ag nanoparticles in response to air (i.e., 0 ppm SO₂) and SO₂ of 1, 5, 25, and 100 ppm concentrations in air were collected as described in Section 3.4. Figure 4.3 shows the extinction spectra of Ag nanoparticles before and after SO₂ injections into the optical cells enclosing the samples (i.e., Ag nanoparticles) for 5 and 100 ppm concentrations. As can be seen from the plot, the extinction peaks were found to instantly broaden as well as decrease in intensity after the samples were exposed to SO₂. Such peak broadenings are attributed to chemical interface damping of the plasmonic oscillations in the nanoparticles that is detailed in Section 2.4.

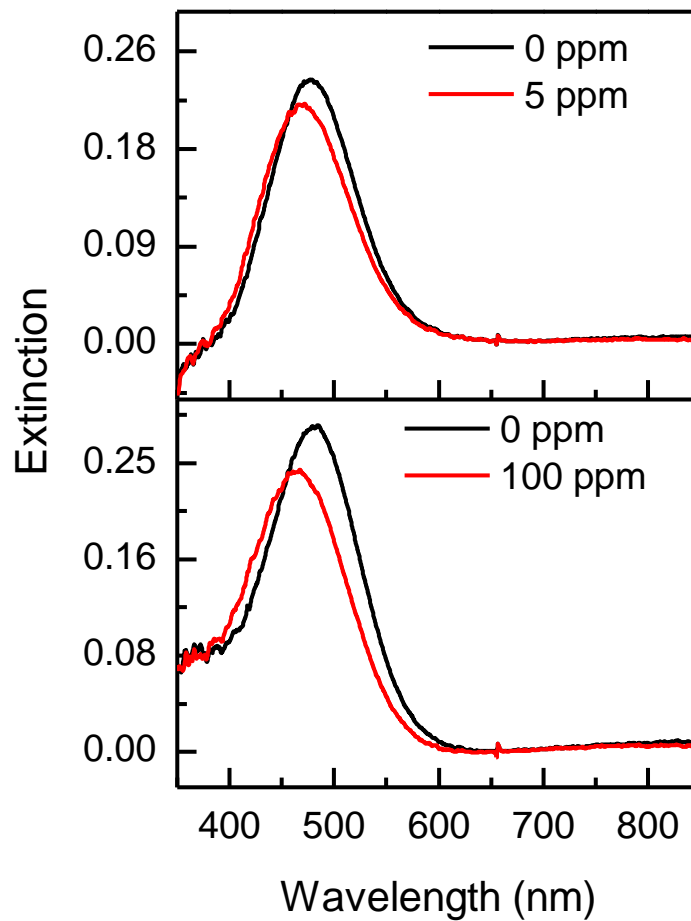


Figure 4.3 Extinction spectra of Ag nanoparticles before (black) and after (red) SO₂ injections of 5 and 100 ppm concentrations, indicative of Ag-SO₂ interaction.

Once the extinction spectra were acquired, the data were exported into Origin 8.1 software. The FWHM of each spectrum was then extracted by fitting the spectral data to the Gaussian function. Subsequently, the change in FWHM (ΔFWHM) between the SO_2 -exposed and the corresponding as-synthesized samples was computed for all SO_2 concentrations. According to the Langmuir's adsorption theory, this change in plasmon damping, (i.e., ΔFWHM) is expected to be linear with the number of SO_2 adsorbates. Thus, the attachment of SO_2 to Ag surface can be modeled by solving the linear differential equation given by

$$\dot{N}_{\text{SO}_2} = (N_a - N_{\text{SO}_2})K_a - N_{\text{SO}_2}K_d \quad (4.1)$$

where \dot{N}_{SO_2} is SO_2 adsorption rate at a given area of Ag surface, N_{SO_2} is the number of SO_2 adsorbates, N_a represents the total number of adsorption sites at the given area, and $K_a = C k_a$ and K_d are adsorption and desorption coefficients, respectively, C being the concentration of SO_2 .

Solving Equation 4.1 yields the saturation adsorption equation (Langmuir isotherm), which is given by

$$N_{\text{SO}_2}(t) = \frac{Ck_a N_a}{Ck_a + K_d} (1 - e^{-(K_a + K_d)t}) \quad (4.2)$$

At saturation (i.e., $t = \infty$), we have

$$N_{\text{SO}_2}(t = \infty) = \frac{Ck_a N_a}{Ck_a + K_d} \quad (4.3)$$

Rewriting Equation 4.3 gives

$$N_{\text{SO}_2}(t = \infty) = \frac{CN_a}{C + \frac{K_d}{k_a}} \quad (4.4)$$

Defining $a = N_a$ and $b = K_d/k_a$ simplifies Equation 4.4 to

$$N_{\text{SO}_2}(t = \infty) = \frac{aC}{C+b} \quad (4.5)$$

which, as noted above, is expected to be directly proportional to the change in damping factor (i.e., $N_{\text{SO}_2}(t = \infty) \propto \Delta\Gamma(t = \infty)$) if damping factor is linearly proportional to the number of SO_2 adsorbates.

The values $a = 0.052 \text{ eV}$ and $b = 2.03 \text{ ppm}$ were determined by fitting Equation 4.5 to the experimental data (i.e., for 1, 5, 25, and 100 ppm SO_2 concentrations). Here, a and b are also the sensor calibration parameters. The change in the damping factor as a function of SO_2 concentration is given in Figure 4.4, where data is also fit (red line) to Equation 4.5. The fitting was performed using Origin 8.1 software. As can be seen in the figure, a good fit (i.e., a standard error of 9×10^{-4}) into the theory was obtained, suggesting that the change in damping ($\Delta\Gamma(t = \infty)$) is indeed linear with the number of SO_2 adsorbates. The error bars in the plot were obtained after 3 replications for each concentration.

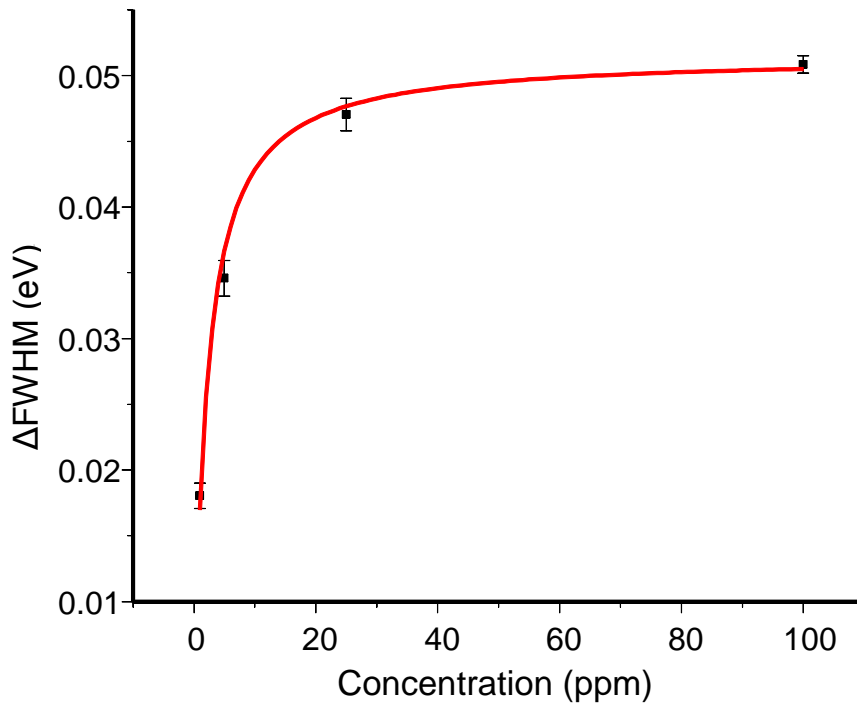


Figure 4.4 Change in plasmon damping factor as a function of SO_2 concentration, and the associated fit (red line) of Equation 4.5.

4.4 SO₂ adsorption to Ag nanoparticles

To verify and elucidate the adsorption of SO₂ to Ag nanoparticles, Raman spectroscopy was performed as described in Section 3.6. Due to the plasmonic surface enhancement of the Raman scattering signal by Ag nanoparticles, the Raman acquisitions essentially represent SERS (Section 2.2). A series of SERS measurements under controlled environment were collected after the sensor chip (i.e., Ag NPs-on-Si-on-glass), or equivalently, the SERS substrate was prepared as shown in Figure 3.2.

First, SERS spectra of the substrate in air and argon were obtained to study the effect of air (i.e., oxygen) in the absence of SO₂ (Figs. 4.5a and 4.5b). Second, SERS spectra of SO₂ in air and SO₂ in argon were collected to determine the effect of oxygen in the presence of SO₂ (Figs. 4.5c and 4.5d). Finally, after 20 min of argon purge and subsequent injection of SO₂, the optical cell was opened to atmosphere for 10 min to let the previously injected SO₂ diffuse out, sealed in Air again, and then SO₂ was injected once more. This step was carried out to study the effect of subsequent oxygen exposures once the substrate surface was first exposed to only SO₂ in Ar (Fig. 4.5e).

In these SERS acquisitions, the substrate was exposed to SO₂ via injection. After injection, the 5 mL internal volume of the cell was filled with 100 ppm SO₂ at total pressure of ~1 atm.

Integration time for all spectra was 200 s except that for SO₂ in air (i.e., Figure 4.5c), which was 10 s due to instability of the signal for longer integration times. All the argon purge steps were conducted for 20 min (i.e., prior to SO₂ injection or SERS acquisition).

Figure 4.5a and 4.5b show representative SERS spectra obtained in air and argon environments, respectively. The spectra show a broad band peaking at 480 cm⁻¹, which is characteristic of the amorphous silicon film underlying the Ag nanoparticles. When SO₂ was injected into the optical cell filled with air, new peaks were emerged at 240, 616, 918 and 960 cm⁻¹ as seen in Figure 4.5c.

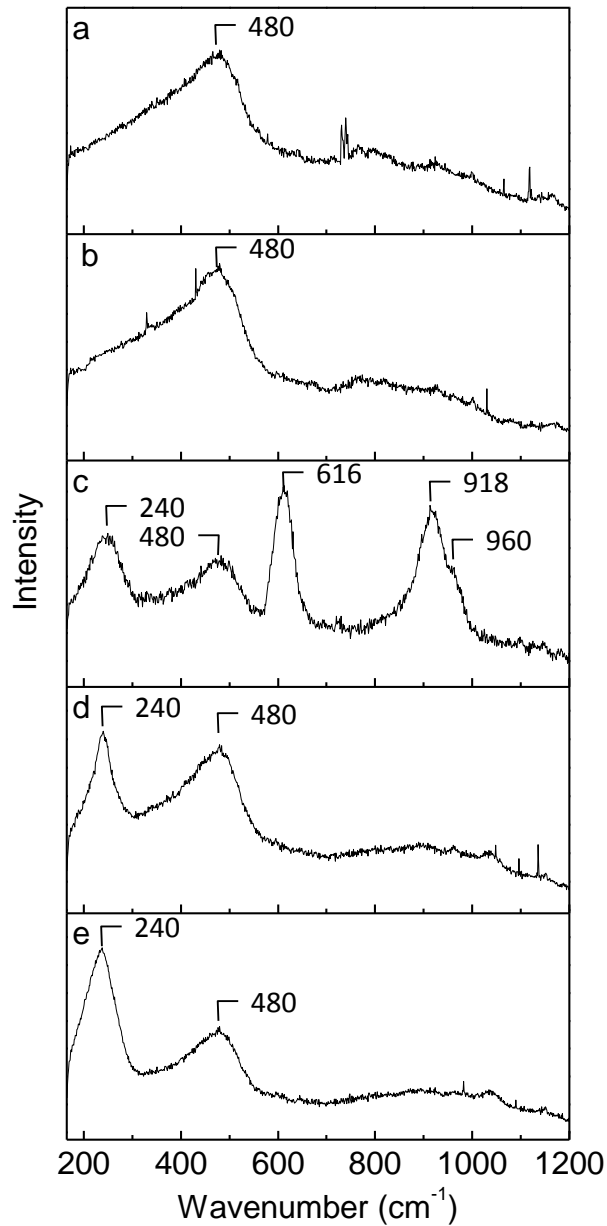


Figure 4.5 SERS spectra obtained from the sensor chip at various exposures: (a) in air; (b) in Ar after 20 min of purge; (c) SO_2 in air; (d) after 20 min of Ar purge and subsequent injection of SO_2 into Ar; and (e) after exposure (d), cell opened to atmosphere for 10 min, sealed again in Air, and then injected with SO_2 .

Interestingly, when SO_2 was injected into argon filled optical cell, only the 240 cm^{-1} peak was observed as presented in Figure 4.5d. In the light of previous reports [92-94], the 616 and 918 cm^{-1} peaks in Figure 4.5c are assigned to S–O bending and stretching modes in SO_3 adsorbed to Ag, while the 240 cm^{-1} peak is ascribed to Ag–S stretch in the Ag– SO_2 adsorption complex.

Hence, these results suggest that SO_2 transforms to SO_3 in the presence of O_2 (i.e., air).

Accordingly, following the work of Outka et al. [92], it is concluded that SO_3 forms when SO_2 adsorbs to atomic oxygen (O) that is already adsorbed to Ag surface.

On the other hand, as mentioned above, no SO_3 Raman peaks were detectable in the absence of atomic oxygen sites on the Ag surface (i.e., when the optical cell was purged with argon).

However, as evidenced from the 240 cm^{-1} peak, SO_2 was able to directly adsorb to Ag surface even if there were no O-sites present. The 240 cm^{-1} peak is assigned to Ag–S bond stretching mode. Figure 4.6 presents a schematic illustration of the two ways whereby the adsorption of SO_2 to Ag surface occurs.

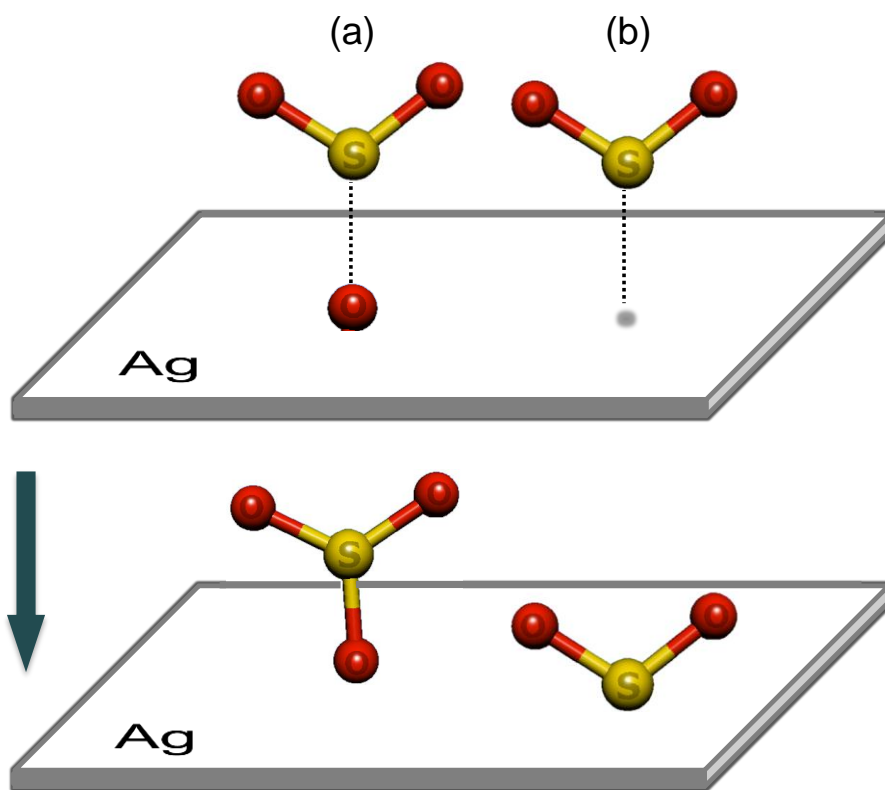


Figure 4.6 Illustration of two different ways of SO_2 adsorption to Ag surface in atmospheric environment: (a) adsorption to adsorbed O forming SO_3 ; (b) direct adsorption.

Figure 4.5e shows the SERS spectrum after the sequential exposures of the substrate to: (i) Ar for 20 min; (ii) SO₂ (100 ppm) for 10 min; (iii) atmosphere for 10 min; and (iv) SO₂ (100 ppm) in air for 10 min. In this final case of investigation, the SO₃ peaks were not detectable. It is inferred, as a result, that atomic oxygen adsorbates did not form on the Ag surface despite exposure to air. This result indicates that once the surface is exposed to only SO₂, essentially all the adsorption sites available to oxygen are invaded by SO₂; and any subsequent exposure to air does not allow O to kick off SO₂ and generate atomic oxygen adsorbates on the Ag surface.

The shoulder peak observed at 960 cm⁻¹, again by following the literature [92, 93, 95], is attributed to adsorbed SO₄²⁻. However, unlike SO₂ and SO₃ adsorbates, the formation of the SO₄²⁻ is understood to be an artifact associated with a photochemical reaction under the 532 nm laser. Figure 4.7 provides time series SERS spectra for the case of 100 ppm SO₂. As can be seen from these time series spectra, the intensity of the 960 cm⁻¹ peak is observed to increase, while the 918 cm⁻¹ peak is fading. This indicates the evolvement of SO₄²⁻ at the expense of SO₃ through a photochemical reaction. Concomitantly, the 616 cm⁻¹ peak was replaced by another peak at 618 cm⁻¹, which is ascribed to bending mode in SO₄²⁻. However, due to the difference in peak positions between the 616 and 618 cm⁻¹ peaks being lower than the peak widths, the replacement was rather observed as a slightly higher energy shift of the 616 cm⁻¹ peak to 618 cm⁻¹. Complete transformation of SO₃ to SO₄²⁻ was seen to occur in about 50 s. Further laser exposure interestingly caused SO₄²⁻ to disappear eventually, possibly due to laser-induced desorption or decomposition.

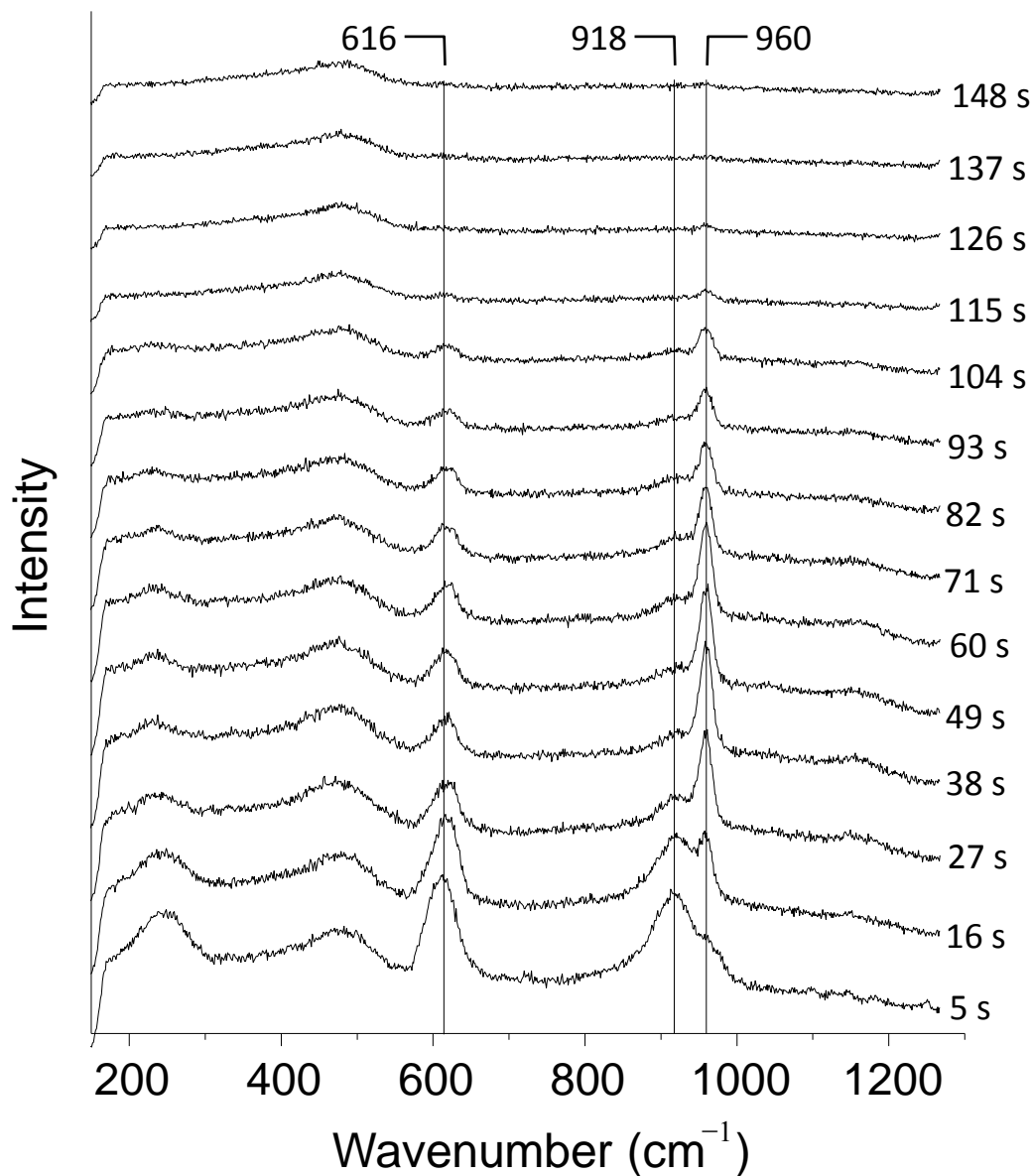


Figure 4.7 Time series SERS spectra acquired after SO_2 injection into the optical cell. The concentration of SO_2 in air is 100 ppm. The spectra are integrated for 10 s, each. A shutter of 1 s is employed between integrations. The time labels in the figure indicate the center of the time interval for the integration. After the 104 s spectrum, every tenth spectrum is shown.

Figure 4.8 shows the integrated intensities of 918 cm^{-1} (SO_3) and 960 cm^{-1} (SO_4^{2-}) peaks as a function of time associated with the time series spectra of Figure 4.7. The integrated peak intensities were obtained after background subtraction and deconvolution of the Raman spectrum into two Voigtian peaks in the $800 - 1100 \text{ cm}^{-1}$ range.

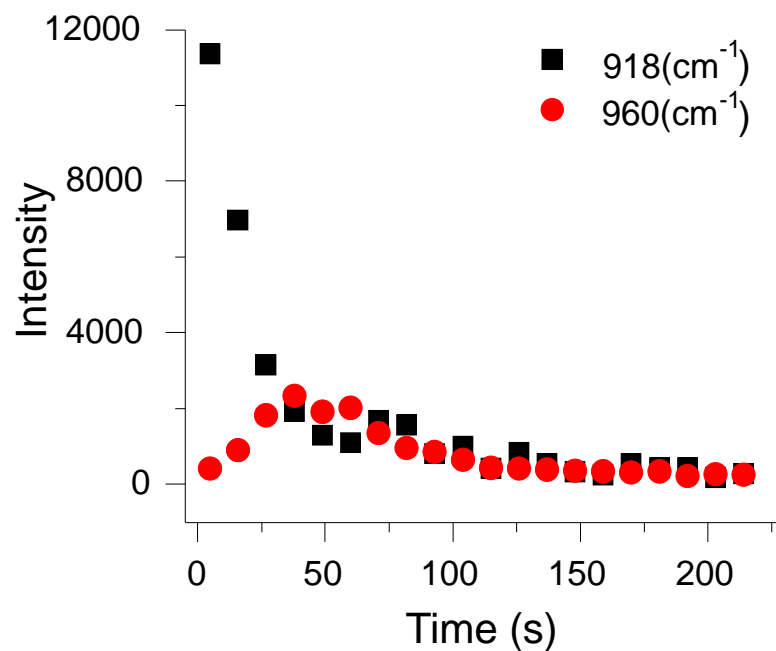


Figure 4.8 Integrated intensities of the 918 cm^{-1} (SO_3) and 960 cm^{-1} (SO_4^{2-}) peaks as a function of time associated with the time series spectra of Figure 4.7.

CHAPTER 5

CONCLUSIONS

The following conclusions are drawn from the results obtained in the present thesis work.

- A simple and low-cost SO₂ nanosensor with sensitivity of as low as 1 ppm has been developed using a monolayer of Ag nanoparticles reduced and immobilized on thin film Si on glass. The sensor exploits hybrid-plasmon damping as the sensing mechanism.
- In addition to sensitivity, the sensor performance has been characterized as: response time < 1 s; accuracy = 94.3 % for 1 ppm, and 98.7 % for 100 ppm.
- It is found that the change in plasmon damping factor ($\Delta\Gamma$) due to SO₂ adsorption is governed by Langmuir adsorption isotherm theory (i.e., the experimental data for $\Delta\Gamma$ vs. concentration were found to fit the Langmuir isotherm equation). This, in turn, leads to a very important conclusion that the $\Delta\Gamma$ must be linearly proportional to the number of SO₂ adsorbates.
- According to the recent work conducted by the Kalkan group [96], the nanosensor developed also detects H₂S. However, the response time is much longer. For 1 ppm H₂S

diluted in H₂ that flows through the optical cell at a flow rate of 520 sccm, the sensor response saturates in 10 s. Hence, compared with H₂S, SO₂ adsorption to Ag is determined to be ultrafast (i.e., < 1 s at 1 ppm) even when there is no associated gas flow.

- As studied by Raman spectroscopy, the adsorption of SO₂ to Ag nanoparticles occurs in two different ways in the presence of O₂. The first one is that SO₂ adsorbs to atomic oxygen (O) that is already adsorbed to the Ag surface (i.e., SO₂ transforms to SO₃ in the presence of O₂). The second one, on the other hand, is that SO₂ attaches directly to the Ag surface. Evidently, the adsorption of SO₂ in the absence of O-sites on the Ag surface occurs only via the second adsorption mode (i.e., by direct attachment of SO₂ to the Ag surface).
- It is also found that once the Ag surface was exposed to only SO₂ essentially all the adsorption sites available to oxygen were invaded by SO₂. In this case, any subsequent exposure to oxygen does not allow O to kick off adsorbed SO₂ and generate atomic oxygen adsorbates on the Ag surface.
- Raman acquisitions with 532 nm excitation laser reveal that the SO₃ adsorbates transform to SO₄²⁻. This SO₄²⁻ evolution is understood to be an artifact associated with a photochemical reaction under the 532 nm laser of the Raman spectrometer. Once SO₃ adsorbates are completely transformed to SO₄²⁻, further laser exposure interestingly causes SO₄²⁻ to also disappear possibly due to laser-induced desorption or decomposition.

REFERENCES

1. Bureau of transportation statistics,
http://www.bts.gov/publications/national_transportation_statistics/2011/html/table_04_01.html. Retrieved 09-13-2012.
2. U. S. energy information administration, Short-term energy outlook, released Sep. 2012.
3. Bureau of transportation statistics,
http://www.bts.gov/publications/national_transportation_statistics/html/table_01_46b.html. Retrieved 09-13-2012.
4. “Pocket guide to transportation,” Bureau of transportation statistics,
http://www.bts.gov/publications/pocket_guide_to_transportation/2012/html/table_03_02.html. Retrieved 09-13-2012.
5. “Air quality criteria for ozone and related photochemical oxidants, EPA/600/P-93/004aF,” U.S. environmental protection agency, (1996).
6. B. Brunekreef, S. T. Holgate, Air pollution and health. *The lancet* **360**, 1233 (2002).
7. C. A. Pope, D. W. Dockery, Health effects of fine particulate air pollution: Lines that connect. *Journal of the air & waste management association* **56**, 709 (2006).
8. D. Nuvolone *et al.*, Geographical information system and environmental epidemiology: a cross-sectional spatial analysis of the effects of traffic-related air pollution on population respiratory health. *Environmental health: A global access science source* **10**, 12 (2011).

9. D. E. Abbey, F. Petersen, P. K. Mills, W. L. Beeson, Long-term ambient concentrations of total suspended particulates, ozone, and sulfur dioxide and respiratory symptoms in a nonsmoking population. *Archives of environmental health* **48**, 33 (1993).
10. G. D. Thurston, K. Ito, Epidemiological studies of acute ozone exposures and mortality. *Journal of exposure analysis and environmental epidemiology* **11**, 286 (2001).
11. D. Malakoff, "Air pollution. Taking the sting out of acid rain," *Science* **330**, 910 (2010).
12. E. U. Liu, C. P. Liu, "Effects of simulated acid rain on the antioxidative system in cinnamomum philippinense seedlings," *Water, air, & soil pollution* **215**, 127 (2011).
13. K. Muthuchelian, N. Nedunchezian, G. Kulandaivelu, "Acid-rain - acidic mist-induced response in growth and photosynthetic activities on crop plants," *Archives of environmental contamination and toxicology* **26**, 521 (1994).
14. E. Rapaport, "The Stockholm environmental zone, a method to curb air pollution from bus and truck traffic," *Transportation research part D-Transport and environment* **7**, 213 (2002).
15. N. P. Hyslop, "Impaired visibility: The air pollution people see," *Atmospheric environment* **43**, 182 (2009).
16. R. T. Burnett *et al.*, Association between ozone and hospitalization for acute respiratory diseases in children less than 2 years of age. *American journal of epidemiology* **153**, 444 (2001).
17. L. Chen, B. L. Jennison, W. Yang, S. T. Omaye, Elementary school absenteeism and air pollution. *Inhalation toxicology* **12**, 997 (2000).
18. F. D. Gilliland *et al.*, The effects of ambient air pollution on school absenteeism due to respiratory illnesses. *Epidemiology (Cambridge, Mass.)* **12**, 43 (2001).
19. "OECD health data 2012," *OECD* (Organization for Economic Co-operation and Development) *Health statistics*, http://stats.oecd.org/index.aspx?DataSetCode=HEALTH_STAT. Retrieved 09-13-2012.
20. "Diesel emission control -- Sulfur effects (DECSE) program; phase I interim data report no. 4: diesel particulate filters—Final report, Jan. 2000" (2008).
21. "Catalyst-based diesel particulate filters and NO_x adsorbers: A summary of the technologies and the effects of fuel sulfur," manufacturers of emission controls association, <http://www.meca.org/galleries/default-file/cbdpf-noxadwp.pdf>. Retrieved 09-14-2012.
22. M. M. Maricq, R. E. Chase, N. Xu, P. M. Laing, The effects of the catalytic converter and fuel sulfur level on motor vehicle particulate matter emissions: light duty diesel vehicles. *Environmental science & technology* **36**, 283 (2002).

23. M. M. Maricq, R. E. Chase, N. Xu, D. H. Podsiadlik, The effects of the catalytic converter and fuel sulfur level on motor vehicle particulate matter emissions: gasoline vehicles. *Environmental science & technology* **36**, 276 (2002).
24. D. M. Serafim, N. R. Stradiotto, Determination of sulfur compounds in gasoline using mercury film electrode by square wave voltammetry. *Fuel* **87**, 1007 (2008).
25. J. Tasheva, P. Petkov, S. Ivanov, Reduction of the contents of sulphur-containing organic compounds, arene hydrocarbons and resinous products in diesel fuels by applying extraction with selective solvents. *Oxidation communications* **27**, 48 (2004).
26. J. A. Valla, A. A. Lappas, I. A. Vasalos, C. W. Kuehler, N. J. Gudde, Feed and process effects on the in situ reduction of sulfur in FCC gasoline. *Applied catalysis A, general* **276**, 75 (2004).
27. U.S. environmental protection agency office of transportation and air quality, "Introduction of cleaner-burning diesel fuel enables advanced pollution control for cars, trucks and buses," EPA420-F-06-037, May 2006.
28. U.S. energy information administration, "The transition to ultra-low sulfur diesel fuel: effects on prices and supply," SR-OIAF/2001-01, May 2001.
29. S. Thind, "Evaluation of sulfur measurements analytical techniques for sulfur in gases and fuel," CI analytical article (**P8-10**), 2 (2004).
30. Department of Energy Archives,
http://www.eia.gov/dnav/pet/hist/LeafHandler.ashx?n=PET&s=WD0TP_NUS_2&f=W. Retrieved 09-15-2012.
31. S. Raimes, The theory of plasma oscillations in metals. *Reports on progress in physics* **20**, 1 (1957).
32. N. Yamamoto, K. Araya, F. J. G. de Abajo, Photon emission from silver particles induced by a high-energy electron beam *Physical review B* **64**, (2001).
33. C. J. Powell, J. B. Swan, Origin of the characteristic electron energy losses in aluminum. *Physical review* **115**, 869 (1959).
34. C. Kittel, *Introduction to solid state physics*. (Wiley, New York, 1986).
35. S. A. Maier, SpringerLink, *Plasmonics: fundamentals and applications* (Springer, New York, 2007), pp. 16 [electronic resource].
36. S. A. Maier, SpringerLink, *Plasmonics: fundamentals and applications* (Springer, New York, 2007). pp. 11 [electronic resource].
37. U. Kreibig, M. Vollmer, *Optical properties of metal clusters* (Springer, New York, 1995), vol. 25. pp. 15.

38. S. A. Maier, SpringerLink, *Plasmonics: fundamentals and applications* (Springer, New York, 2007). pp. 10 [electronic resource].
39. A. Campion, P. Kambhampati, Surface-enhanced Raman scattering. *Chemical society reviews* **27**, 241 (1998).
40. N. Shuming, R. E. Steven, Probing single molecules and single nanoparticles by surface-enhanced Raman scattering. *Science* **275**, 1102 (1997).
41. R. L. McCreery, Raman spectroscopy for chemical analysis. *Measurement science and technology* **12**, 653 (2001).
42. P. Mulvaney, Surface plasmon spectroscopy of nanosized metal particles. *Langmuir* **12**, 788 (1996).
43. S. Underwood, P. Mulvaney, Effect of the solution refractive-index on the color of gold colloids. *Langmuir* **10**, 3427 (1994).
44. A. J. Haes *et al.*, Plasmonic materials for surface-enhanced sensing and spectroscopy. *Mrs bulletin* **30**, 368 (2005).
45. P. Nordlander, C. Oubre, E. Prodan, K. Li, M. I. Stockman, Plasmon hybridization in nanoparticle dimers. *Nano letters* **4**, 899 (2004).
46. P. Mulvaney, Not all that's gold does glitter. *Mrs bulletin* **26**, 1009 (2001).
47. S. Connolly, S. Cobbe, D. Fitzmaurice, "Effects of ligand-receptor geometry and stoichiometry on protein-induced aggregation of biotin-modified colloidal gold," *J Phys Chem B* **105**, 2222 (2001).
48. C. Haynes, R. Van Duyne, "Nanosphere lithography: A versatile nanofabrication tool for studies of size-dependent nanoparticle optics," *J Phys Chem B* **105**, 5599 (2001).
49. C. A. Mirkin, R. L. Letsinger, R. C. Mucic, J. J. Storhoff, "A DNA-based method for rationally assembling nanoparticles into macroscopic materials," *Nature* **382**, 607 (1996).
50. Biological sensor based on localized surface plasmon associated with surface-bound Au/polystyrene composite microparticles, (2004).
51. A. Henglein, D. Meisel, "Spectrophotometric observations of the adsorption of organosulfur compounds on colloidal silver nanoparticles," *J Phys Chem B* **102**, 8364 (1998).
52. M. Malinsky, K. Kelly, G. Schatz, R. Van Duyne, "Chain length dependence and sensing capabilities of the localized surface plasmon resonance of silver nanoparticles chemically modified with alkanethiol self-assembled monolayers," *J. Am. Chem. Soc.* **123**, 1471 (2001).

53. M. Sanekata, I. Suzuka, "Physical and chemical interface effects on Mie plasmon absorption of sodium nanoclusters passivated with $\text{CH}_4\text{-nCl}_n$ ($n = 1\text{-}4$) molecules," *Chemical physics letters* **323**, 98 (2000).
54. I. Tokarev, I. Tokareva, V. Gopishetty, E. Katz, S. Minko, Specific biochemical-to-optical signal transduction by responsive thin hydrogel films loaded with noble metal nanoparticles. *Advanced materials (Deerfield Beach, Fla.)* **22**, 1412 (2010).
55. W. P. Hall, S. N. Ngatia, R. P. Van Duyne, LSPR biosensor signal Enhancement using nanoparticle-antibody conjugates. *Journal of physical chemistry C* **115**, 1410 (2011).
56. P. B. Johnson, R. W. Christy, Optical Constants of the Noble Metals. *Physical review B* **6**, 4370 (1972).
57. I. Freestone, N. Meeks, M. Sax, C. Higgitt, The Lycurgus cup — A Roman nanotechnology. *Gold bulletin* **40**, 270 (2007).
58. C. Dahmen, G. von Plessen, Optical effects of metallic nanoparticles. *Australian journal of chemistry* **60**, 447 (2007).
59. <http://www.discovernano.northwestern.edu/whatis/History/HistoryPopup>.
60. M. Faraday, The bakerian lecture: experimental relations of gold (and other metals) to light. *Philosophical transactions of the royal society of London* **147**, 145 (1857).
61. U. Kreibig, M. Vollmer, *Optical properties of metal clusters*. (Springer, New York, 1995), vol. 25. pp. 31.
62. S. Eustis, M. A. El-Sayed, Why gold nanoparticles are more precious than pretty gold: noble metal surface plasmon resonance and its enhancement of the radiative and nonradiative properties of nanocrystals of different shapes. *Chemical society reviews* **35**, 209 (2006).
63. S. S. Agasti *et al.*, Nanoparticles for detection and diagnosis. *Advanced drug delivery reviews* **62**, 316 (2010).
64. X. H. Huang, P. K. Jain, I. H. El-Sayed, M. A. El-Sayed, Gold nanoparticles: interesting optical properties and recent applications in cancer diagnostic and therapy. *Nanomedicine* **2**, 681 (2007).
65. P. K. Jain, I. H. El-Sayed, M. A. El-Sayed, Au nanoparticles target cancer. *Nano today* **2**, 18 (2007).
66. C. Loo, A. Lowery, N. Halas, J. West, R. Drezek, Immunotargeted nanoshells for integrated cancer imaging and therapy. *Nano letters* **5**, 709 (2005).
67. M. Arruebo, R. Fernández-Pacheco, M. R. Ibarra, J. Santamaría, Magnetic nanoparticles for drug delivery. *Nano today* **2**, 22 (2007).

68. R. Singh, J. J. W. Lillard, Nanoparticle-based targeted drug delivery. *Experimental and molecular pathology* **86**, 215 (2009).
69. N. L. Rosi, C. A. Mirkin, Nanostructures in biodiagnostics. *Chemical reviews* **105**, 1547 (2005).
70. A. J. Haes, W. P. Hall, L. Chang, W. L. Klein, R. P. Van Duyne, A localized surface plasmon resonance biosensor: first steps toward an assay for alzheimer's disease. *Nano letters* **4**, 1029 (2004).
71. I. H. El-Sayed, X. Huang, M. A. El-Sayed, Surface plasmon resonance scattering and absorption of anti-EGFR antibody conjugated gold nanoparticles in cancer diagnostics: applications in oral cancer. *Nano letters* **5**, 829 (2005).
72. K. Sokolov *et al.*, Real-time vital optical imaging of precancer using anti-epidermal growth factor receptor antibodies conjugated to gold nanoparticles. *Cancer research* **63**, 1999 (2003).
73. <http://www.thenanoera.com/>
74. A. Y. Vlasov, Quantum information science and nanotechnology (2009).
75. P. Vettiger *et al.* (The institute of electrical and electronics engineers, inc. (IEEE), Piscataway), vol. 1, pp. 39.
76. S. Wakeland *et al.*, Multilayered nanoparticles generated by plasma methods for energy storage applications. *Nanoscience and nanotechnology letters* **4**, 316 (2012).
77. K. Q. Peng, X. Wang, X.-L. Wu, S.-T. Lee, Platinum nanoparticle decorated silicon nanowires for efficient solar energy conversion. *Nano letters* **9**, 3704 (2009).
78. E. Prodan, C. Radloff, N. J. Halas, P. Nordlander, A Hybridization model for the plasmon response of complex nanostructures. *Science* **302**, 419 (2003).
79. P.K. Jain, S. Eustis, M.A. El-Sayed, *J. Phys. Chem. B* **110**, 18243 (2006).
80. A. K. Kalkan, "Hybrid plasmon damping sensor," US Patent Application 12/347,771, (2010).
81. C. Sönnichsen., Thesis Ludwig-Maximilians-Universität München (2001).
82. P. K. Jain, M. A. El-Sayed, Noble metal nanoparticle pairs: effect of medium for enhanced nanosensing. *Nano letters* **8**, 4347 (2008).
83. P. K. Jain, M. A. El-Sayed, Plasmonic coupling in noble metal nanostructures. *Chemical physics letters* **487**, 153 (2010).
84. B. N. J. Persson, Polarizability of small spherical metal particles - influence of the matrix environment. *Surface science* **281**, 153 (1993).

85. H. Hövel, S. Fritz, A. Hilger, U. Kreibig, M. Vollmer, Width of cluster plasmon resonances: Bulk dielectric functions and chemical interface damping. *Physical review B* **48**, 18178 (1993).
86. U. Kreibig, Interface-induced dephasing of Mie plasmon polaritons. *Applied physics B* **93**, 79 (2008).
87. F. Hubenthal, C. Hendrich, F. Träger, Damping of the localized surface plasmon polariton resonance of gold nanoparticles. *Applied physics B* **100**, 225 (2010).
88. J. Bosbach, C. Hendrich, F. Stietz, T. Vartanyan, F. Träger, Ultrafast dephasing of surface plasmon excitation in silver nanoparticles: influence of particle size, shape, and chemical surrounding. *Physical review letters* **89**, 257404 (2002).
89. U. Kreibig, M. Gartz, A. Hilger, Mie resonances: Sensors for physical and chemical cluster interface properties. *Berichte der bunsen-gesellschaft-physical chemistry chemical physics* **101**, 1593 (1997).
90. F. G. Lether and P. R. Wenston, "The numerical computation of the Voigt function by a corrected midpoint quadrature rule for $(-\infty, \infty)$," *Journal of computational and applied mathematics* **34**, 75 (1991).
91. <http://mattson.creighton.edu/HowToPrepGases/Index.html>. Retrieved 10-05-2012.
92. D. A. D. A. Outka, R. J. Madix, G. B. Fisher, C. DiMaggio, Oxidation of sulfur dioxide on Ag (110): Vibrational study of the structure of intermediate complexes formed. *J. phys. chem* **90**, 4051 (1986).
93. P. B. Dorain, K. U. Vonraben, R. K. Chang, B. L. Laube, Catalytic formation of SO_3^{2-} and SO_4^{2-} from SO_2 on silver observed by surface-enhanced Raman scattering. *Chemical physics letters* **84**, 405 (1981).
94. H. Matsuta, SERS observation of the adsorption behavior of SO_2 on silver powder surfaces at nearly real environmental conditions. *Applied surface science* **27**, 482 (1987).
95. T. T. Chen, K. U. Von Raben, D. V. Murphy, R. K. Chang, B. L. Laube, Surface enhanced raman scattering and second-harmonic generation from CN^- complexes and SO_2^{-4} on Ag electrodes during oxidation-reduction cycles. *Surface science* **143**, 369 (1984).
96. Rama Krishna Rao Gowd Ede, "Plasmon-damping chemical sensor for hydrogen fuel monitoring," Thesis, (2011).

VITA

Eli Kasa Tilahun

Candidate for the Degree of

Master of Science

Thesis: SO₂ DETECTION USING PLASMON DAMPING

Major Field: Mechanical and Aerospace Engineering

Biographical:

Education:

Completed the requirements for the Master of Science in Mechanical and Aerospace Engineering at Oklahoma State University, Stillwater, Oklahoma in December, 2012.

Completed the requirements for the Bachelor of Science in Mechanical Engineering at Arba Minch University, Arba Minch, Ethiopia in 2006.

Experience:

Worked as Design Engineer Intern at Total valve systems in Broken Arrow, Oklahoma

Worked as Research Assistant in the Functional Nanomaterials Laboratory at Oklahoma State University in Stillwater, Oklahoma

Worked as Erection Engineer I at Ethiopian Electric Power Corporation Gilgel Gibe II project in Gilgel Gibe, Ethiopia

Worked as Engineer Trainee at Fincha Sugar Factory in Fincha, Ethiopia

Worked as Design Engineer Intern at Akaki Spare Parts and Hand Tools S.C. in Addis Ababa, Ethiopia

Professional Memberships:

Student Member of American Society of Mechanical Engineers

Certifications:

Engineer in Training (EIT) Certification
Certified SolidWorks Associate (CSWA)